



# Optimization of critical process control parameters in MEX additive manufacturing of high-performance polyethylenimine: energy expenditure, mechanical expectations, and productivity aspects

Nectarios Vidakis<sup>1,3</sup> · Markos Petousis<sup>1</sup> · Mariza Spiridaki<sup>1</sup> · Nikolaos Mountakis<sup>1</sup> · Amalia Moutsopoulou<sup>1</sup> · Emmanuel Kymakis<sup>2,3</sup>

Received: 23 November 2023 / Accepted: 10 March 2024 / Published online: 19 March 2024

© The Author(s) 2024

## Abstract

The demand for 3D-printed high-performance polymers (HPPs) is on the rise across sectors such as the defense, aerospace, and automotive industries. Polyethyleneimine (PEI) exhibits exceptional mechanical performance, thermal stability, and wear resistance. Herein, six generic and device-independent control parameters, that is, the infill percentage, deposition angle, layer height, travel speed, nozzle temperature, and bed temperature, were quantitatively evaluated for their impact on multiple response metrics related to energy consumption and mechanical strength. The balance between energy consumption and mechanical strength was investigated for the first time, contributing to the sustainability of the PEI material in 3D printing. This is critical considering that HPPs require high temperatures to be built using the 3D printing method. PEI filaments were fabricated and utilized in material extrusion 3D printing of 125 specimens for 25 different experimental runs (five replicates per run). The divergent impacts of the control parameters on the response metrics throughout the experimental course have been reported. The real weight of the samples varies from 1.06 to 1.82 g (71%), the real printing time from 214 to 2841 s (~ 1300%), the ultimate tensile strength from 15.17 up to 80.73 MPa (530%), and the consumed energy from 0.094 to 1.44 MJ (1500%). The regression and reduced quadratic equations were validated through confirmation runs (10 additional specimens). These outcomes have excessive engineering and industrial merit in determining the optimum control parameters, ensuring the sustainability of the process, and the desired functionality of the products.

**Keywords** Polyethyleneimine (PEI) · ULTEM™ · Material extrusion (MEX) 3D printing · Mechanical response · Energy consumption · Robust design

## Nomenclature

3D-P	Three-dimensional printing	$D_A$	Deposition angle
AM	Additive manufacturing	DOF	Degree of freedom
ANOVA	Analysis of variance	DSC	Differential scanning calorimetry
BBD	Box–Behnken design	$D_T$	Total degree of freedom
CNF	Cellulose nanofiber	$E$	Tensile modulus of elasticity
CQI	Critical quality indicators	$E_{PC}$	Energy printing consumption
		FDM	Fused deposition modeling

✉ Nectarios Vidakis  
vidakis@hmu.gr

Markos Petousis  
markospetousis@hmu.gr

Mariza Spiridaki  
mspyridaki@hmu.gr

Nikolaos Mountakis  
mountakis@hmu.gr

Amalia Moutsopoulou  
amalia@hmu.gr

Emmanuel Kymakis  
kymakis@hmu.gr

<sup>1</sup> Department of Mechanical Engineering, Hellenic Mediterranean University, 71410 Heraklion, Greece

<sup>2</sup> Department of Electrical & Computer Engineering, Hellenic Mediterranean University (HMU), 71410 Heraklion, Crete, Greece

<sup>3</sup> Institute of Emerging Technologies (I-EMERGE) of HMU Center for Research & Development, 71410 Heraklion, Crete, Greece

FFD	Full factorial design
FFF	Fused filament fabrication
HPPs	High-performance polymers
IM	Injection molded
$I_p$	Infill percentage
$L_H$	Layer height
LRM	Linear regression model
MEP	Main effect plot
MEX	Material extrusion
PA12	Polyamide 12
PC	Polycarbonate
PEEK	Polyetheretherketone
PEI	Polyetherimide
PEKK	Polyetherketoneketone
PPSU	Polyphenylsulfone
$P_T$	Printing time
PVDF	Polyvinylidene fluoride
QRM	Quadratic regression model
RQRM	Reduced quadratic regression model
SEM	Scanning electron microscopy
$S_{PE}$	Specific printing energy
$S_{PP}$	Specific printing power
$SS_E$	Sum of squared errors
$SS_p$	Sum of squared deviations
$SS_T$	Total sum of squares
$S_T$	Travel speed
$T_B$	Bed temperature
TD	Taguchi design
TGA	Thermogravimetric analysis
$T_N$	Nozzle temperature
$T_t$	Tensile toughness
ULTEM	Trade name of polyetherimide
UTS	Ultimate tensile strength
$V_p$	Variance of parameter
VPP	Vat photopolymerization
$W_s$	Specimen weight
$\sigma_B$	Tensile strength

## 1 Introduction

High-performance polymers (HPPs) for AM are utilized in MEX 3D printing, also known as fused filament fabrication (FFF), to produce a wide variety of parts. The use of HPPs in AM has advantages over traditional manufacturing methods in terms of efficiency, cost-effectiveness, and sustainability [1, 2]. Among the HPPs, the most adopted are polyetherimide (PEI, usually called by its trade name ULTEM™), polyetheretherketone (PEEK), polyetherketoneketone (PEKK), polyvinylidene fluoride (PVDF), and polyphenylsulfone (PPSU) [3]. These HPPs were introduced as upgraded alternatives to commodities and/or engineering polymers for AM, which are usually restricted

by accuracy issues and limited thermomechanical performance [4, 5]. PEI was introduced by the General Electric Company as a polymer with higher strength, even at elevated temperatures, making it suitable for applications in which resistance to creep is a requirement [6]. PEEK has similar mechanical specifications but is also suitable for medical applications [7]. PEKK is similar to PEEK, but has a lower melting point, making it easier to process [8, 9]. PVDF exhibits piezoelectric properties [10], whereas PPSU is primarily used in membranes and foams [11–13].

It should be noted that HPPs need to be 3D printed under relatively high processing temperatures (nozzle, table, and chamber) [14]. Apart from the high processing temperatures, the main drawbacks of using HPPs in AM are related to the material costs and scalability [15]. Overcoming these challenges shows potential opportunities for broader adoption of HPPs in various industries [16]. HPPs can find engineering applications in fields such as medicine (as implant materials) [17], chemicals, electronics, transportation, energy, marine, and construction, as well as in defense and aerospace industries [3, 18–20]. Non-load-bearing applications in airbuses include airflow ducts, brackets, clips, and electrical boxes, which are suitable for high-performance polymers (HPPs) [21].

Efforts have also been made to introduce HPPs to the oil and gas industry, where there are high heat conditions and corrosive environments; hence, there is a need for high material strength and industrial safety [3]. Their remarkable performance is a corollary of the stability they are provided with, when found under extreme conditions, with their durability lasting for extended periods of time [19, 20]. In addition to their notable mechanical properties, HPPs are characterized by thermal stability and high and continuous resistance to temperature, chemicals, wear, and flames [22].

Cost-effectiveness and environmental safety are two current issues that occupy the industrial and research domains [23]. Some studies have investigated energy consumption versus strength in the MEX 3DP of polylactic acid [23, 24], as well as compressive [25] and tensile [26] responses versus power consumption in the case of acrylonitrile butadiene styrene. The energy consumption for manufacturing parts using the 3D printing method versus their mechanical strength has also been studied for polycarbonate [27], poly[methyl methacrylate] (PMMA) [28], and polyamide 6 (PA6) [29] polymers. In these studies, an optimum set of 3D printing parameters that minimized the energy consumption and maximized the mechanical performance was the aim.

Consequently, it is also vital to investigate HPPs that enable lightweight structures [30] for their power consumption/absorption when 3D printed. It should be noted that, to the best of the authors' knowledge, there are limited studies on energy consumption and part weight. However, similar

to the common polymers used in 3D printing [31–34], several investigations have been conducted on the mechanical properties of HPPs [35, 36].

Regarding the energy consumption of HPPs in 3D printing, which contributes to the eco-friendliness and sustainability profile of the materials, there was an investigation combining the energy consumption and tensile strength metrics of PEEK in MEX 3DP with three key process control parameters, utilizing the Box–Behnken modeling approach [37]. In another study, the mechanical behavior, modeling behavior, and energy absorption of short carbon fiber-reinforced PEEK composites were investigated [38]. Carbon fibers reinforced with PEEK composite hot isostatic pressing have been investigated to improve their mechanical properties [39].

Polyetherimides (PEI) are amorphous, transparent, or amber HPP and are widely known for their commercial name ULTEM™. It has remarkable mechanical, thermal, and chemical properties that make it suitable for applications that require high temperatures and harsh environments. PEI has a polyamide composition with ether linkages in the aromatic polymer backbone, which is responsible for its satisfactory rheology and consequently its good melt processability while maintaining its thermal and mechanical properties under challenging conditions [40].

PEI's glass transition temperature of PEI is reported to be 217 °C [40, 41], and when utilized in conventional melt processing methods, it can reach 350 to 425 °C [40]. In addition, even at 450–500 °C PEI was thermally stable. The onset thermal degradation of PEI is not affected by the nature of the atmosphere, except in an oxidative environment where PEI degradation is effectuated in two rapid steps. Notably, the 1- and 10-year TGA service life temperatures were 318 °C and 292 °C, respectively [40].

PEI can resist chemical attacks from substances such as hydrocarbons, alcohols, and halogenated solvents. They can also retard flames and emit extremely low levels of smoke [21]. The mechanical properties of ULTEM™ are influenced by process parameters, such as layer or building orientations [42].

Numerous studies have been conducted on the behavior of PEI composites and their suitability in various fields, such as PEI/carbon fibers [43], PEI/glass fabrics with three weaves [44], PEI/graphite nanoplatelets [45], PEI/cross-ply glass fibers [46], and PEI/LCP/polyphosphazene [47].

The commercial PEI appearing in the literature in most cases is ULTEM™ 9085 [48], whereas ULTEM™ 1010, ULTEM™ 1000, and ULTEM™ 5000 are occasionally used. In the literature, as will be presented below, the examined control parameters, as well as the responses, varied, highlighting factors and settings with remarkable effects. The full factorial design (FFD) of the experiment was mostly used for the analysis, while Doehlert or Taguchi designs were also

employed. ULTEM™ 9085 was utilized, in a study examining the fabricated specimens under the control parameters of time, print direction, temperature, and annealing over the responses of UTS, % strength compared to IM parts, and the strain measured at break [49]. With the assistance of an L9 design based on the Taguchi method, this study demonstrated that longer and higher annealing temperatures improved the mechanical metrics. In another study, a commercial ULTEM™ 1010 filament was used. The fabricated specimens were chosen as control parameters for the layer height, raster angle, air gap, and direction of the building, with the tensile strength, UTS, and Young's modulus set as the responses [50]. By engaging a two-level full factorial design, the study showed that the air gap mainly affects the UTS and modulus of elasticity, whereas the build direction affects Young's modulus and tensile strain at break.

A commercial ULTEM™ 9085 filament was used to examine the fabricated specimens by selecting the orientation of the layers and the direction of the building control parameters with tensile and flexural strengths as responses [42]. The study proved that the edge-printing direction yields increased levels of strength with the assistance of the Design-Expert software (v. 11). A commercial ULTEM™ 9085 filament was also utilized in a study in which the fabricated specimens were examined under the control parameters of build orientation with responses of tensile strength, strength utilization, elasticity modulus, and strain to failure [51]. The study showed that a flat build orientation in the Z-direction led to higher values for all mechanical metrics.

Another study utilized a commercial ULTEM™ 9085 filament and examined the responses of strain, flexural modulus, and strength of the fabricated specimens under the control parameters of temperature, time, pressure, printing orientations, and annealing process [52]. With the assistance of a Doehlert design, the study showed that samples undergoing annealing in an environment under pressure developed a higher flexural modulus and strength, as well as reduced surface roughness. The investigators of another study used MEX 3DP processed polycarbonate and commercial ULTEM™ 9085 compounds and examined the fabricated specimens by setting the control parameters of temperature, pressure, thickness reduction, and layer orientations with responses to the density before hot pressing, density after hot pressing, and ultimate strength [53]. Their study showed that higher temperatures led to lower porosity and higher ultimate strength after hot pressing.

Taylor et al. used a ULTEM™ 1010 filament and examined the MEX fabricated specimens setting as control parameters, temperature, print orientation, raster angle, and air gap, with yield strength and modulus as the response parameters [54]. Employing a full factorial design, this study showed that an increase in temperature decreases the modulus of elasticity and yield strength. Taylor et al. added

raster and contour widths to the control parameter ensemble and examined the conditional critical stress intensity factor, which was proved to be affected by the raster angle [55]. Chueca de Bruijn et al. used a ULTEM™ 9085 filament and examined the fabricated specimens under the control parameters of the infill pattern, air gap, wall thickness, cell geometry, and build direction with responses to the stiffness and maximum load [56]. The study reported that building parts without support structures resulted in increased stiffness.

In another study, researchers used commercial ULTEM™ 1010 filaments and examined the fabricated specimens under the control parameters of raster angles and multiorientated layers, examining the response strength and hardness [57]. The study showed that multiorientation leads to higher tensile stresses. Additionally, Yilmaz et al. utilized commercial ULTEM™ 1010 filaments and MEX 3DP specimens, selecting the raster angle and annealing temperature as control parameters, while the metrics were the elongation at break, hardness, and tensile strength [58]. The authors claimed that higher annealing temperatures resulted in an increased hardness.

In Gebisa and Lemu's investigations, ULTEM™ 9085 commercial filament was utilized to fabricate specimens with control parameters, such as the air gap, raster deposition width, angle, and number of contours, and their width with flexural strain, strength, and modulus, as well as tensile strength and tensile strain as the response metrics [59]. The results showed that the raster angle and width had significant effects on the flexural strength, modulus, and strain.

In a study by Glaskova-Kuzmina et al., commercial ULTEM™ 9085 was utilized for the fabrication of specimens under the control parameters of 3D printing orientation and post-printing cooling temperatures, with response parameters of flexural strength, modulus, tensile strength, and elastic modulus [60, 61]. The results showed that the cooling temperature did not affect the static and fatigue bending properties, whereas post-printing cooling at room temperature reduced the tensile strength and elastic modulus.

Mzabi et al. utilized a ULTEM™ 1000 filament to produce test specimens, setting the temperature and frequency as control parameters, and the measured heat flow, absorbance, and current were the response metrics [62]. Fabrizio et al. used a commercial ULTEM™ 1000 filament to produce specimens by selecting the bed temperature, layer thickness, fan speed, IR power levels, geometry, orientation, and raster angle with the response parameters of warping and overheating [63]. Higher control parameter levels have been shown to prevent warping.

Motaparti et al. fabricated specimens with commercial ULTEM™ 9085 filaments, with the direction of the building, air gap, raster angle, and temperature as control parameters and the yield strength, strength/mass, modulus/mass, and flexural modulus as the response outcomes [64]. Using a

full factorial design modeling method, it was proven that the vertical direction exhibits a higher yield strength. Gómez-Gras et al. utilized a ULTEM™ 9085 filament and fabricated specimens by adjusting the diameter, build direction, feed rate, and cutting speed in milling and examining their roughness and dimensional deviations [65]. By utilizing a full factorial design, it was found that the cutting speed influenced the  $R_A$  (average roughness) and  $R_T$  (height of the profile (RT) roughness metrics).

Padovano et al. fabricated specimens from a commercial ULTEM™ 9085 filament and determined the control parameters of the build direction, temperature, humidity, and density based on the yield strength, UTS, elasticity modulus, and strain observed at break [66]. The building direction had a strong impact on the tensile and flexural properties. Han et al. utilized a commercial ULTEM™ 1010 filament to fabricate specimens with control parameters of layer height, extrusion width and temperature, bed and chamber temperature, nozzle speed, filament diameter, raft, and laser power (used for filament preheating) [67]. The response parameter was the tensile strength, and it was proven that a high laser power yielded a higher ultimate tensile strength.

Kaplun et al. utilized commercial ULTEM™ 9085 to 3D print specimens, choosing as control parameters raster infill patterns, layer height, nozzle and chamber temperature, and printing speed [68]. Shelton et al. fabricated specimens via thermal processing using a ULTEM™ 9085 filament. The control parameters were moisture, glass transition temperature of the exposed filament, build dog bone, dog bone after dry-out, and melt flow index [69]. The response parameters were ultimate tensile strength, elastic modulus, and failure strain. The authors claimed that a lower moisture content leads to a higher modulus and strength.

In the available literature, there are studies of similar interest as this study, which conclude with various results. As previously mentioned, high envelope temperatures lead to high ultimate strength values and improved consistency [70]. Forés-Garriga et al. [71] investigated three control parameters and determined a high level of strength for edge-created specimens. Chueca de Bruijn et al. [72] studied the control parameters of chemical treatment and proved that the tensile and flexural strengths increased with the addition of particular solvents.

Moreover, according to Ding et al. [73], high nozzle temperatures can improve the density levels. McLouth et al. [74] demonstrated that the adhesive strength was improved by atmospheric plasma treatment. Ahmad and Ezdeen [5, 75] noted the influence of an increased coating thickness on the ultimate tensile strength and Young's modulus. Fischer and Schöppner [76] concluded that chemical smoothing of parts built in an upright orientation leads to a higher ultimate tensile strength, whereas Bagsik et al. [77] proved that a negative air gap and thick filaments provide better mechanical

properties. Krause et al. [78] imply that the thickness affects isothermal potential decay.

Popular experimental designs include the full factorial design (FFD), Box–Behnken design (BBD), and Taguchi design (TD). In this study, the Taguchi design was chosen. FFD has been applied in studies such as the comprehensive investigation of the mechanical response resulting from the 3D printing control settings on polycarbonate (PC) [79]. Moreover, N. Vidakis et al. utilized an FFD on Polyamide 12 (PA12) with three different control parameters, with the aim of investigating its strength and toughness [80]. In addition, the process modeling of the TPU's FFF mechanical response under the control parameters of layer height and nozzle temperature [81] or the PLA nanocomposites investigated the effects of laser-cutting parameters [82].

The building of this experiment was based on the Taguchi experimental design, which helped organize and develop the investigation, as well as the whole procedure and the evaluation of the results from the findings. Orthogonal arrays are helpful in parameter studies for minimizing the required number of experiments [83]. The choice of orthogonal arrays is affected by the total number of degrees of freedom ( $D_T$ ), which represents the number of factors subtracting one [84] and is supposed to be less than the  $D_T$  of the chosen orthogonal array.

The TD is also utilized to analyze the influence of various parameters on the objective function, as well as their capability to solve a problem, resulting in the greatest combination of parameters [85]. Its proven success [86–90] has contributed to its applications in several research fields [91]. This method suggests the most suitable order of independent parameters according to their importance for dependent objective functions [92] while defining a summary of the parameters, which will be used to produce the best-case and worst-case scenarios.

Moreover, the Taguchi design was successfully adopted in the study by Vidakis et al. [93] who conducted research on biomedical resins for VPP-3D printing, reinforced with nanofibers of cellulose (CNF), investigating the effect of filler content, as well as geometric control parameters on critical quality indicators (CQIs), employing a Taguchi L9 orthogonal array. In another study [94], the Taguchi design was one of the three experimental modeling approaches tested (full factorial and Box–Behnken were the other two designs). They were used for mechanical strength predictability to optimize the thermal settings and cellulose nanofiber content in PA12 for MEX. These methods, along with the analysis of variance, have proven to be sufficient and effective for analyzing and optimizing experimental data [95]. Other modeling tools, such as artificial neural networks (ANN), have also been employed [96, 97]. The literature review findings are summarized in Table 1.

In the existing literature on PEI in MEX AM, there is an obvious lack of a systematic multiparametric assessment of the key generic, that is, 3D printer vendor, model, and size-independent control settings, and their impact on critical productivity, environmental, and performance metrics, at once and correlated with each other. Moreover, most researchers have engaged commercial PEI filaments without thorough, yet essential, material documentation, owing to the trade secrets of their vendors. Finally, owing to their limited experimental runs, previous investigations examined control parameters and levels and did not offer massive sets of experimental metrics, were able to produce robust predictive equations, or could be exploited in multiobjective optimization assessments. The present study aims to fill this gap in the literature by elaborating a concrete, reliable, and reproducible experimental course, along with a coherent assessment of the derived response metrics and evolved descriptive statistics.

As shown in the literature review above, the study of 3D printing parameters for the enhancement of the performance of parts built with this method is of great interest, and often diverse results have been reported [98–100]. Herein, for the first time, a fine powder of PEI was utilized to produce a high-standard filament at a laboratory scale with varying specifications and thermomechanical features to evaluate the energy required to build a part using the MEX 3D printing method. The motivation for studying PEI among HPPs is related to the relatively lower cost of the polymer compared to the remaining HPPs, along with its mechanical performance. These qualities make the polymer a cost-efficient one among the HPPs.

To the best of the authors' knowledge, the quantification of energy metrics to build parts with HPPs using the MEX 3D printing method has not been presented previously in the literature. Apart from the quantification of the energy consumed to build a part, the effects of six critical and generic 3D printing parameters on both the energy consumption and mechanical performance of the parts produced using the MEX method were assessed. This approach aimed to propose a balance between the energy consumption and mechanical performance of parts produced with PEI using the MEX 3D printing method. This balance has merit, especially for the PEI HPP, considering the high temperature required to build the parts, which is expected to require higher energy amounts during the 3D printing process. An orthogonal L25 experimental design was developed, including six generic continuous control parameters: infill percentage ( $I_p$ ), deposition angle ( $D_A$ ), layer height ( $L_H$ ), travel speed ( $S_T$ ), nozzle temperature ( $T_N$ ), and bed temperature ( $T_B$ ), with five suitable levels for each parameter. Hereby, 25 experimental runs were prepared with five repetitions (replicates) of each run (125 experimental sets in total). The L25 experimental design was selected because a corresponding

**Table 1** Literature on the research on the mechanical and other properties of PEI

Study	Filament	Responses	Remarkable effect of the factors
(El Magri et al., 2021) [5]		Tensile strength Young modulus	
(Byberg et al., 2018) [42]	ULTEM 9085®	Tensile strength Flexural strength	Edge printing direction shows high levels of strength
(Hajjiha et al., 2020) [48]	ULTEM 9085®	Tensile strength Compressive strength Shear strength Poisson ratio Elastic modulus Longitudinal tensile strain Void volume ratio	
(Zhang & Ki Moon, 2021) [49]	ULTEM 9085®	Ultimate tensile strength (MPa) % of IM Strain at break	Longer and higher annealing temperature improves mechanical properties
(Pandelidi et al., 2021) [50]	ULTEM 1010	Tensile strength Young modulus Strain at break	Air gap affects tensile strength and Young modulus, build direction affects Young modulus and tensile strain at break
(Zaldivar et al., 2017) [51]	ULTEM 9085®	Tensile strength (MPa) Strength utilization (FDM/ injection molded) (%) Modulus (GPa) Strain-to-failure (%)	Flat in the Z direction built orientation shows higher values of all mechanical properties
(Chueca de Bruijn et al., 2023) [52]	Ultem™ 9085	Flexural modulus Flexural strength Strain	Samples annealed in a pressurized environment present higher flexural modulus and flexural strength and lower surface roughness
(Parker et al., n.d.) [53]	FDM processed polycarbonate and ULTEM 9085 provided by Stratasys	Density before hot pressing Density after hot pressing Ultimate strength	Higher temperatures lead to lower porosity after hot pressing and higher ultimate strength
(Taylor et al., 2018) [54]	Ultem 1010	Yield strength Modulus	Increase in temperature causes a decrease in modulus and yield strength
(Taylor et al., 2019) [55]	ULTEM 1010	The conditional critical stress intensity factor	Raster angle affects the conditional critical stress intensity factor
(Chueca de Bruijn et al., 2022) [56]	Ultem™ 9085	Change in stiffness Change in max load	Built without support showed an increase in stiffness
(Yilmaz & Yilmaz, 2022) [57]	ULTEM 1010 (PEI developed by Stratasys Ltd.)	Stress Hardness	Multiorientation leads to higher tensile stresses
(Yilmaz et al., 2022) [58]	Polyetherimide (PEI/ULTEM 1010) polymer	Elongation at break Hardness Tensile stress	Higher annealing temperature provides higher values of hardness
(Gebisa and Lemu, 2019) [59]	ULTEM 9085®	Tensile strength Tensile strain	Lower raster angle gives higher tensile strength and strain
(Glaskova-Kuzmina et al., 2023) [60]	ULTEM® 9085	Tensile strength Elastic modulus Maximal deformation	Post printing cooling at room temperature causes reduction of tensile strength and elastic modulus

**Table 1** (continued)

Study	Filament	Responses	Remarkable effect of the factors
(Glaskova-Kuzmina et al., 2023) [61]	ULTEM® 9085 provided by Stratasys (Eden Prairie, MN, USA)	Flexural strength Flexural modulus Maximal strain	Oven cooling temperature does not affect static and fatigue bending properties
(Mzabi et al., 2009) [62]	Polyetherimide (Ultem 1000)	Heat flow Absorbance Current Warping Overheating	Heating favors physical aging decreases dipole mobility and stabilizes charges in deeper energetic levels Higher temperature levels prevent warping
(Fabrizio et al., 2022) [63]	ULTEM™ 1000 pellets	Yield strength Strength/mass Modulus/mass Flexural modulus	Vertical build direction exhibits high yield strength
(Motaparti et al., 2017) [64]	Ultem 9085	Roughness Deviation	Cutting speed influenced Ra and Rt roughnesses
(Gómez-Gras et al., 2021) [65]	ULTEM® 9085	Yield strength Ultimate tensile strength Elastic modulus Elongation at break	Building direction has an effect on tensile and flexural properties
(Padovano et al., 2020) [66]	Ultem 9085	Tensile strength Elastic modulus (GPa) Failure strain (%)	High laser power shows higher ultimate tensile strength
(Han et al., 2019) [67]	Black Ultem 1010 (PEI Ultem 1010 black, 3DXTech, Grand Rapids, USA)	Modulus Strength Strain	Edge orientation shows higher strength and failure strain values
(Kaplan et al., 2020) [68]	ULTEM 9085®	Ultimate strength (MPa) Ultimate strength COV (%) Yield stress (MPa) Elastic modulus (GPa) Strain-to-failure (%)	Higher envelope temperatures lead to high values of ultimate strength and improved consistency
(Shelton et al., 2020) [69]	Ultem 9085 (3DXTECH, Grand Rapids, MI, USA)	Tensile moduli Flexural moduli Shear moduli Poisson ratio	Edge-created specimens show higher levels of strength
(Forés-Garriga et al., 2020) [71]	ULTEM 9085®	Mass loss % treatment Tensile modulus Tensile strength Strain at tensile Flexural modulus Flexural strength	Tensile and flexural strength increase by adding particular solvents
(Chueca de Bruijn et al., 2020) [72]	Ultem™ 9085		

Table 1 (continued)

Study	Filament	Responses	Remarkable effect of the factors
(Ding et al., 2019) [73]	PEI 1010 (Junhua China)	Density Flexural strength Tensile strength Breaking elongation Impact strength	Increase of nozzle temperature improves density levels
(McLouth et al., 2021) [74]	ULTEM® 9085	Contact angle Tensile stress Oxygen o/c ratio Relative composition	Adhesive strength is improved by atmospheric plasma treatment
(Ahmad & Ezdeen, 2023) [75]	ULTEM 1010	Modulus of elasticity Ultimate tensile strength Damping loss factor	Increase of coating thickness causes an increase in ultimate tensile strength and Young's modulus
(Fischer & Schöppner, 2017) [76]	ULTEM 9085®	Ultimate strength Elongation at break	Injection molded built orientation shows higher ultimate tensile strength
(Bagsik et al., 2011) [77]	Ultem 9085	Tensile strength Tensile strain at break	Negative air gap and thick filaments give better mechanical properties
(Krause et al., 1998) [78]	Ultem 1000, Ultem 5000	Isothermal potential decay TSC current	Thickness affects the isothermal potential decay

full factorial design would require  $5^6 = 15.625$  experiments to be implemented, which is not feasible in the context of such a scientific study. In addition to the predictability of the impact of the selected ensemble of control settings and the corresponding equations presented below, the findings prove that parameters that significantly affect energy expenditure do not necessarily have any significant impact on the mechanical response of the workpieces and vice versa. The experimental analysis employing statistical modeling tools led to the formation of prediction models, to estimate critical metrics related to energy consumption and the mechanical performance for the manufacturing of PEI parts with the 3D printing method. These prediction models proved their accuracy with a confirmation run and constitute a road map for selecting the proper 3D printing setting, according to the specifications of each application and they are ready to be applied in real-life applications. The objectives of the research are summarized as follows:

- Quantify the energy consumed when 3D printing PEI parts with the MEX method.
- Estimate the effect of six generic 3D printing parameters on the energy consumption and the mechanical performance of PEI 3D printed parts.
- Exploration for a set of 3D printing settings that will minimize the consumed energy and maximize the mechanical performance of the fabricated parts.
- Form reliable prediction models for the energy and mechanical performance metrics, which can be used as a road map for the design of industrial processes, related to the fabrication of PEI parts with the MEX 3D printing method.

## 2 Materials and methods

Figure 1 depicts the total process followed for the aim of this experimental work. The raw material (PEI) was sourced in powder form, and it was initially dried in an industrial oven (Fig. 1b). The dried powder was fed in a filament extruder (Fig. 1b) to produce 1.75 mm filament, compatible with the MEX 3D printing process, which underwent a further drying process (Fig. 1c), before it was used for the 3D printing of the specimens, due to the fact that the filament extrusion and the 3D printing process were not carried out on the same day. Specimens were fabricated with the MEX 3D printing process (Fig. 1d). During the 3D printing process, the energy consumption was monitored (Fig. 1e). The fabricated specimens underwent quality control (Fig. 1f) and then they were tested for their mechanical performance (Fig. 1g). The morphological characteristics of the samples, after their failure in the experimental procedure, were examined with



SEM (Fig. 1h). This process, briefly presented in Fig. 1, is analytically presented below.

## 2.1 Materials

The matrix material used in this study was polyetherimide (PEI) (Goodfellow Cambridge Limited, Huntingdon PE29 6WR England) in the form of a natural-colored powder. The data table provided by the vendor claims that the density is  $1.27 \text{ g/cm}^3$ , tensile modulus is 2.9 GPa, tensile strength is 85 MPa, elongation at break is 60%, and the Poisson ratio is 0.44, respectively.

## 2.2 Fabrication of filaments and specimens along with testing of their mechanical properties

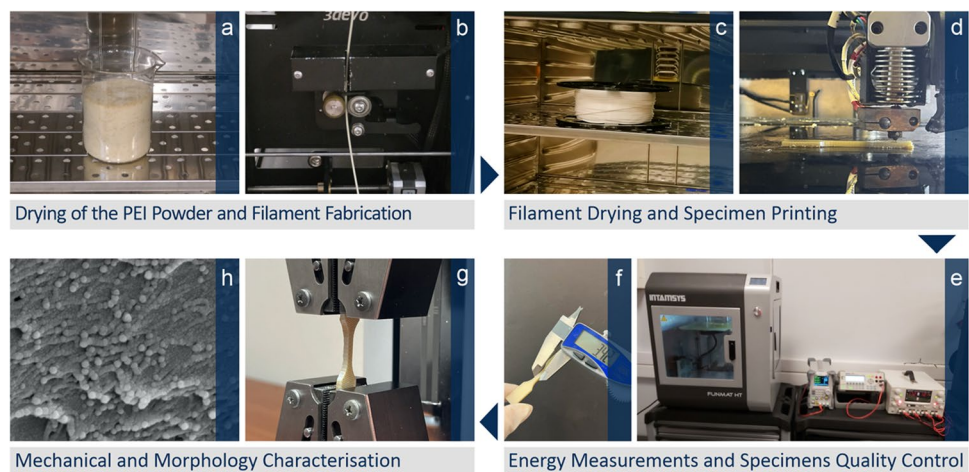
Pure PEI in powder form was extruded in filament form engaging a single-screw Composer series extruder (3devo BV) from Netherlands' Utrecht (diameter of filament: 1.75 mm, setting in first heat zone:  $330 \text{ }^\circ\text{C}$ , in second heat zone:  $340 \text{ }^\circ\text{C}$ , in third heat zone:  $350 \text{ }^\circ\text{C}$ , and in fourth heat zone:  $360 \text{ }^\circ\text{C}$ ), in order to be utilized for the production of specimens. The diameter of the filament was monitored to ensure compliance with the standards throughout melt extrusion fabrication. The fabrication of specimens was conducted through MEX 3DP using a Funmat HT series MEX 3D Intamsys device (Intamsys, Shanghai, China), according to the desired values of the control parameters, which can be found in Figure S1 of the supplementary information. The fabricated specimens were subjected to tensile testing (according to the ASTM D638-02a international standard) to form an image of their mechanical behavior using a model MX2 Imanda device (Imanda Inc., IL, USA) equipped with two standard grips.

## 2.3 TGA, DSC

The key thermal properties were determined using TGA and DSC. Thermogravimetric analysis was performed to depict the thermal behavior of the specimens using a Diamond PerkinElmer TG/TDA device (PerkinElmer, Massachusetts, USA). During the analysis, a nitrogen atmosphere was used, while the temperature fluctuated from 0 up to  $800 \text{ }^\circ\text{C}$ , and the heating rate was set at  $10 \text{ }^\circ\text{C}/\text{min}$ . For DSC, the apparatus TA-Instruments DSC 25 (TA, Instruments from New Castle, United States) was utilized at a heating of  $25\text{--}460 \text{ }^\circ\text{C}$  and a  $10 \text{ }^\circ\text{C}$  heating step.

By observing the TGA graph (Fig. 2a), it is observed that the weight loss did not decrease until the temperature reached  $400 \text{ }^\circ\text{C}$  and then dropped sharply when the temperature reached  $420 \text{ }^\circ\text{C}$ . The filament extrusion and 3D printing nozzle temperatures are presented in the graphs. It is shown that the temperatures in the current study are lower than the temperature that causes acute degradation of the PEI polymer. Therefore, such behavior did not occur in the subsequent process, as it would influence the mechanical properties acquired during the experimental procedure. As for the information extracted from the DSC graph (Fig. 2b), it is noticeable that the heat lowers at higher temperatures, while there is a phase transition as the temperature ranges from  $205$  to  $212 \text{ }^\circ\text{C}$ . Through the thermal property investigation, as mentioned, it was assured that the temperatures for the filament extrusion and the 3D printing process do not cause any degradation in the samples; thus, the provided experimental results are not affected by such phenomena. At the same time, the provided thermal behavior of the PEI polymer can be considered when using the polymer in applications, in which the parts operate in an environment with high temperatures. This is a common application of the HPPs, as presented in the “Introduction” section.

**Fig. 1** Depiction of the steps followed during the experimental procedure, **a** drying process of the PEI powder, **b** fabrication and **c** drying of filament, **d** specimen printing, **e** measurement of energy consumption, **f** quality control of specimens, **g** mechanical characterization, and **h** morphological characterization



## 2.4 Specimens' morphology, SEM analysis, optical microscopy, and stereoscopy examination

To examine the morphology of the specimens, SEM, optical microscopy, and stereoscopy were utilized. SEM was performed by capturing images with a field-emission device, Jeol JSM-IT700HR (Jeol, Tokyo, Japan), while the samples were precoated with Au to prevent charging effects. The device was adjusted to high-vacuum mode and an acceleration voltage of 20 kV. In addition to the quality, the fusion between the strands was examined for the side surface of the specimens, and their fracture faces were also examined in terms of fracture patterns after the mechanical tests. The microscopic inspection was performed using an optical microscope (Kern OKO-1, Germany) and an OZR5 stereoscope, both featuring a digital camera (ODC 832 5 MP, KERN & SOHN GmbH, Germany). Images were captured from the upper surface of the specimens (optically), their side surfaces (optically), and their fracture edges (stereoscopic).

## 2.5 Documentation of energy consumption

During the fabrication of 3DP specimens, energy consumption was measured and recorded by a Rigol DM-3058E (RIGOL Technologies, Shanghai, China) digital multimeter, choosing a “start-counting-stop” approach. The assessment started from the machine's startup, continued during the 3DP process, and ended when the machine was shut down.

The equations used for the calculation of the total energy consumption  $E_{\text{total}}$  were

$$E_{\text{total}} = E_{\text{thermal}} + E_{\text{motion}} + E_{\text{auxiliary}} \quad (1)$$

where

$$E_{\text{thermal}} = E_{\text{heating}} + E_{\text{cooling}} \quad (2)$$

$E_{\text{heating}}$  is the energy required for the heating of the peripherals of the 3D printer (extrusion head, etc.) and  $E_{\text{cooling}}$  is the

energy consumed after the build of the part is completed to cool the peripherals of the 3D printer before it shuts down.

$E_{\text{motion}}$  refers to the energy absorbed by the motors of the 3D printer, their various electronics, and their peripheral features, and finally  $E_{\text{auxiliary}}$  is the remaining consumed energy not included in the above categories. This energy is required to operate the 3D printing machine and it is consumed in all three stages, at the 3D printer startup ( $E_{\text{startup}}$ ), the part manufacturing state ( $E_{\text{steadystate}}$ ), and the shutdown state ( $E_{\text{shutdown}}$ ):

$$E_{\text{auxiliary}} = E_{\text{startup}} + E_{\text{steadystate}} + E_{\text{shutdown}} \quad (3)$$

To normalize the energy metrics, the specific printing energy ( $S_{\text{PE}}$ ) was introduced as

$$S_{\text{PE}} = \frac{E_{\text{PC}}}{W_{\text{S}}} \left[ \frac{\text{MJ}}{\text{g}} \right] \quad (4)$$

while the specific printing power ( $S_{\text{PP}}$ ) metric was yielded from

$$S_{\text{PP}} = \frac{E_{\text{PC}}}{P_{\text{T}} \cdot W_{\text{S}}} \left[ \frac{\text{W}}{\text{g}} \right] \quad (5)$$

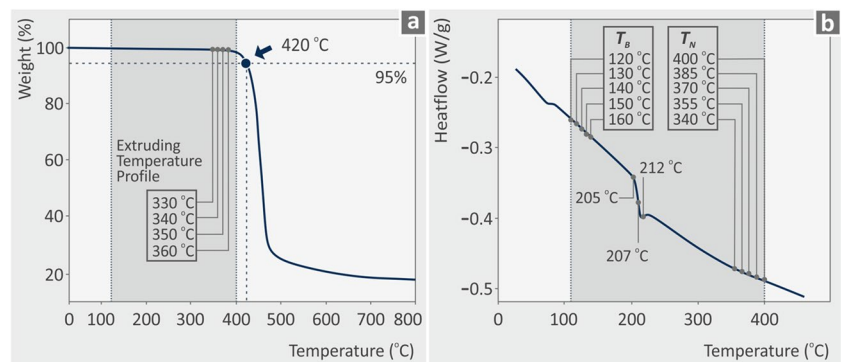
Here,  $E_{\text{PC}}$  represents the overall energy printing consumption used by the 3D printer ( $E_{\text{total}}$ ),  $W_{\text{S}}$  represents the actual weight of each specimen, and  $P_{\text{T}}$  is the actual printing time of each experimental run.

## 2.6 Orthogonal L25 experimental design

The Taguchi method includes a formulation course with signal-to-noise ( $S/N$ ) calculation of ratios for each factor under question, the ratio calculation of delta values from  $S/N$ , and each factor's order (the so-called rank) determination. Three different criteria rank the  $S/N$  ratio: the larger the value, the better the lower, and the better the nominal value [101]. The corresponding formula is as follows:

Larger is better [102]:

**Fig. 2** Graph of **a** weight (%) versus temperature (°C) (TGA) and **b** heat flow (W/g) versus temperature (°C) (DSC) for PEI



$$S/N = -10\log\left(\frac{1}{n} \sum_{i=1}^n \frac{1}{Y_i^2}\right) \tag{6}$$

Smaller is better[90]:

$$S/N = -10\log\left(\frac{1}{n} \sum_{i=1}^n Y_i^2\right) \tag{7}$$

Nominal is best [103, 104]:

$$S/N = 10\log\left(\frac{\mu^2}{\sigma^2}\right) \tag{8}$$

where  $\mu$  refers to the mean,  $\sigma$  is the standard deviation, and  $Y_i$  corresponds to the resulting value of the  $i_{th}$  objective function. The calculation computes delta values through the difference between the highest and lowest  $S/N$  metrics for each parameter and then ranks them. The highest delta value is considered the most effective control setting, and the ranks are depicted in this order.

The selected design was an L25 orthogonal array including 25 experimental runs, with five repetitions for each of them, forming a massive experimental volume with 125 sets of responses. Six 3DP control parameters were used in this robust design: infill percentage ( $I_p$ ) (%), deposition angle ( $D_A$ ) ( $^\circ$ ), layer height ( $L_H$ ) (mm), travel speed ( $S_T$ ) (mm/s), nozzle temperature ( $T_N$ ) ( $^\circ\text{C}$ ), and bed temperature ( $T_B$ ) ( $^\circ\text{C}$ ). Table 2 summarizes the set of 3D printing control parameters along with their respective levels. The levels were chosen through preliminary screening tests as well as through the literature research presented in the ‘‘Introduction’’ section above.

Corresponding modeling of the Taguchi L25 orthogonal array design methodology was also utilized in the study by Vidakis et al. [105] for the investigation of polylactic acid, with six key process parameters in MEX 3DP, as well as for the optimization of key quality indicators in MEX 3DP for acrylonitrile butadiene styrene [106]. In this study, eight response metrics were evaluated and optimized using this approach. Four metrics related to the mechanical performance of the samples, that is, tensile strength  $\sigma_B$  (MPa), tensile modulus of elasticity  $E$  (MPa), tensile toughness  $T_t$  (MJ/m<sup>3</sup>), and sample weight  $W_S$  (g), and four metrics related to the energy consumption (i.e., overall energy printing consumption ( $E_{PC}$ ) (MJ), specific printing energy ( $S_{PE}$ ) (MJ/g), specific printing power ( $S_{PP}$ ) (W/g), and printing time  $P_T$  (s)) were assessed. With this approach, the effects of the control parameters on both mechanical performance and energy consumption were investigated. The aim was to locate the optimum set of parameter levels for the mechanical metrics, energy metrics, or even a possible set of parameter levels that optimizes both the mechanical and energy responses of the

PEI 3D printed samples. The control parameters were ranked according to their importance for each response metric.

### 2.7 Analysis of variance (ANOVA)

ANOVA is a descriptive statistical approach suitable for analyzing experimental results to highlight and distinguish the factors with the strongest impact on the outcomes, as follows:

The  $SS_T$  (total sum of squares) is calculated [107]:

$$SS_T = \sum_{i=1}^N (Y_i - \bar{Y})^2 \tag{9}$$

Here,  $N$  is the case number within the orthogonal array,  $Y_i$  is the numerical or experimental outcome for the  $i_{th}$  experimental case, and

$$\bar{Y} = \frac{1}{N} \sum_{i=1}^N Y_i \tag{10}$$

The  $SS_T$  (total sum of the squared deviations) (SST) is derived from the  $SS_e$  (sum of the squared error) (SSE) and the  $SS_p$  (sum of the squared deviations) (SSP) due to each process parameter; therefore,  $SS_p$  was defined as [107]

$$SS_p = \sum_{j=1}^t \frac{(SY_j)^2}{t} - \frac{1}{N} \left[ \sum_{i=1}^N Y_i \right]^2 \tag{11}$$

where  $P$  is one of the parameters,  $j$  is the parameter’s  $P$  level number,  $t$  is the parameter’s  $P$  repetition at each level, and  $SY_j$  is the sum of the experimental results involving parameters  $P$  and  $j$ . The  $SS_e$  (sum of squares from the error parameters (SSE) is [107]

$$SS_e = SS_T - SS_A - SS_B - SS_C - SS_D - SS_E \tag{12}$$

The total degree of freedom was  $D_T = N - 1$ , and the degree of freedom of each tested parameter was  $D_p = N - 1$ .

The variance of the parameters tested was  $V_p = SS_p/D_p$ . The  $F$  value for each design parameter is simply the ratio of the mean of squares deviations to the mean of the squared error  $F_p = V_p/V_e$ . The percentage contribution,  $\rho_p$ , was calculated as [107]

$$\rho_p = \frac{SS_p}{SS_T} \tag{13}$$

ANOVA was used to compile prediction models for each response metric, as a function of the control parameters studied. The reliability of these prediction models was estimated by calculating the respective  $R$  values. Additionally,

**Table 2** TD L25: control parameters, along with their levels

Run	$I_p$ (%)	$D_A$ (deg)	$L_H$ (mm)	$S_T$ (mm/sec)	$T_N$ (°C)	$T_B$ (°C)
1	60	0.0	0.10	10	340	120
2	60	22.5	0.15	25	355	130
3	60	45.0	0.20	40	370	140
4	60	67.5	0.25	55	385	150
5	60	90.0	0.30	70	400	160
6	70	0.0	0.15	40	385	160
7	70	22.5	0.20	55	400	120
8	70	45.0	0.25	70	340	130
9	70	67.5	0.30	10	355	140
10	70	90.0	0.10	25	370	150
11	80	0.0	0.20	70	355	150
12	80	22.5	0.25	10	370	160
13	80	45.0	0.30	25	385	120
14	80	67.5	0.10	40	400	130
15	80	90.0	0.15	55	340	140
16	90	0.0	0.25	25	400	140
17	90	22.5	0.30	40	340	150
18	90	45.0	0.10	55	355	160
19	90	67.5	0.15	70	370	120
20	90	90.0	0.20	10	385	130
21	100	0.0	0.30	55	370	130
22	100	22.5	0.10	70	385	140
23	100	45.0	0.15	10	400	150
24	100	67.5	0.20	25	340	160
25	100	90.0	0.25	40	355	120

two confirmation runs were carried out (one with the optimum control parameter values for the energy metrics and one with the respective values for the mechanical property metrics), to further evaluate the accuracy of the prediction models, by comparing the actual and the predicted response metric values.

### 3 Results

#### 3.1 Morphological characterization

Figure 3 presents images of the upper surface of the fabricated specimens (one randomly selected sample from each of the 25 runs) captured by the optical microscope, as well as their various control/3D printing parameters. It is noticeable that the 3D structure of each run's supplement differs because of the different 3DP parameters. It should be mentioned that runs 4 and 7 seem to present some bubbles along the layer fusion, while run 25 shows less well-distributed fusion layering, which means that there is still some room for improvement regarding the settings.

The rest of the runs presented a great layer fusion without voids or defects, characterized by uniformity, indicating the appropriation of their applied settings.

Figure 4 shows the mechanical test and morphological analysis results from further investigation of the selected runs (after a random selection of specimens among the five produced for every run), specifically runs 1, 7, 13, 19, and 25. Figure 4a–e shows the graphs of stress vs. strain after the tensile tests of each run, along with the respective tensile strength ( $\sigma_B$ ) (MPa) and toughness ( $T_t$ ) ( $\text{MJ/m}^3$ ) values. It can be observed that the highest toughness value is found in the case of run 19 ( $T_t = 9.1 \text{ MJ/m}^3$ ) along with the highest value of tensile strength ( $\sigma_B = 63.0 \text{ MPa}$ ). It also had the second-highest strain at failure, showing a more ductile response than the other samples, except for run 1. The high strain at failure, along with the highest tensile strength, explains the higher tensile toughness among the examined runs. Run 1 exhibited the lowest tensile strength among all the runs. The specific sample showed the most ductile behavior, as it failed at a higher strain than that in the remaining runs.

Figure 4 also depicts SEM images of the samples' side surfaces, which show a great fusion layering, except for the case of run 13 (Fig. 4c), where some gaps appear between the layers. The most uniform fusion was observed in run 1. Figure 4f–j presents the SEM fracture surface images of the corresponding runs mentioned above, all at  $\times 30$  magnification. The layer fusion appeared to be mostly well-distributed. Run 7 showed a more brittle failure with lower

deformation than the remaining runs, which was also verified by the lower strain at the failure of the sample. At the same time, the specific sample showed larger internal voids in the structure, which can be attributed to the failure of the sample in the tests. The fracture surface of run 19, which had the highest mechanical performance, was rather solid, with smaller internal voids. The structure showed deformation, which is in agreement with the high strain of the sample at failure. It should be noted that run 7 shows the more brittle behavior among the runs presented. The ductile or brittle failure mechanism is not connected to the mechanical strength. Regarding the tensile toughness, it is

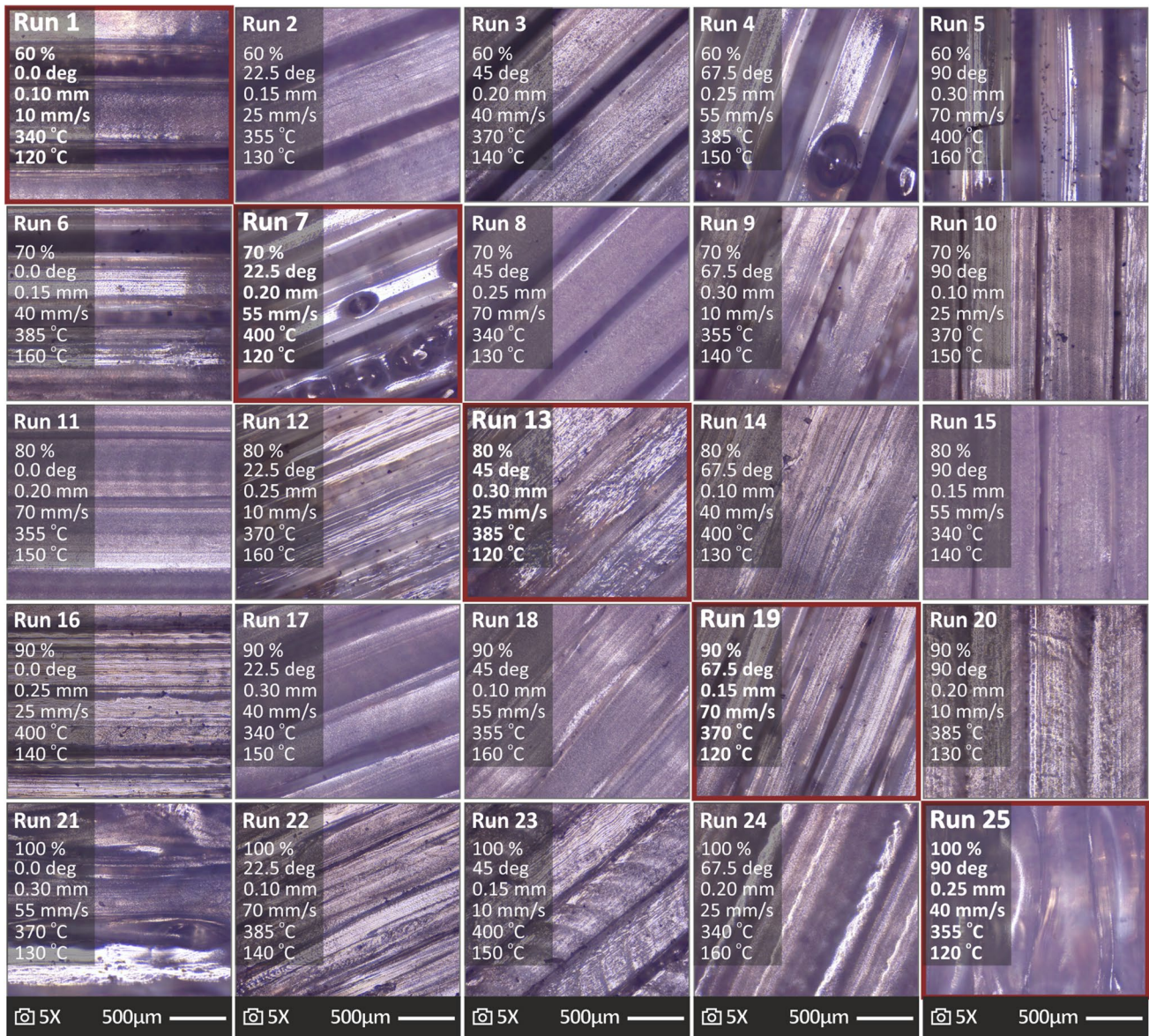


Fig. 3 Depiction of the specimens' upper surface for the 25 runs (a randomly selected sample from each run), fabricated according to different 3D printing parameters, captured by a microscope. The param-

eters are presented in every case. Red frames portray the diagonal runs that are used as indicative ones below

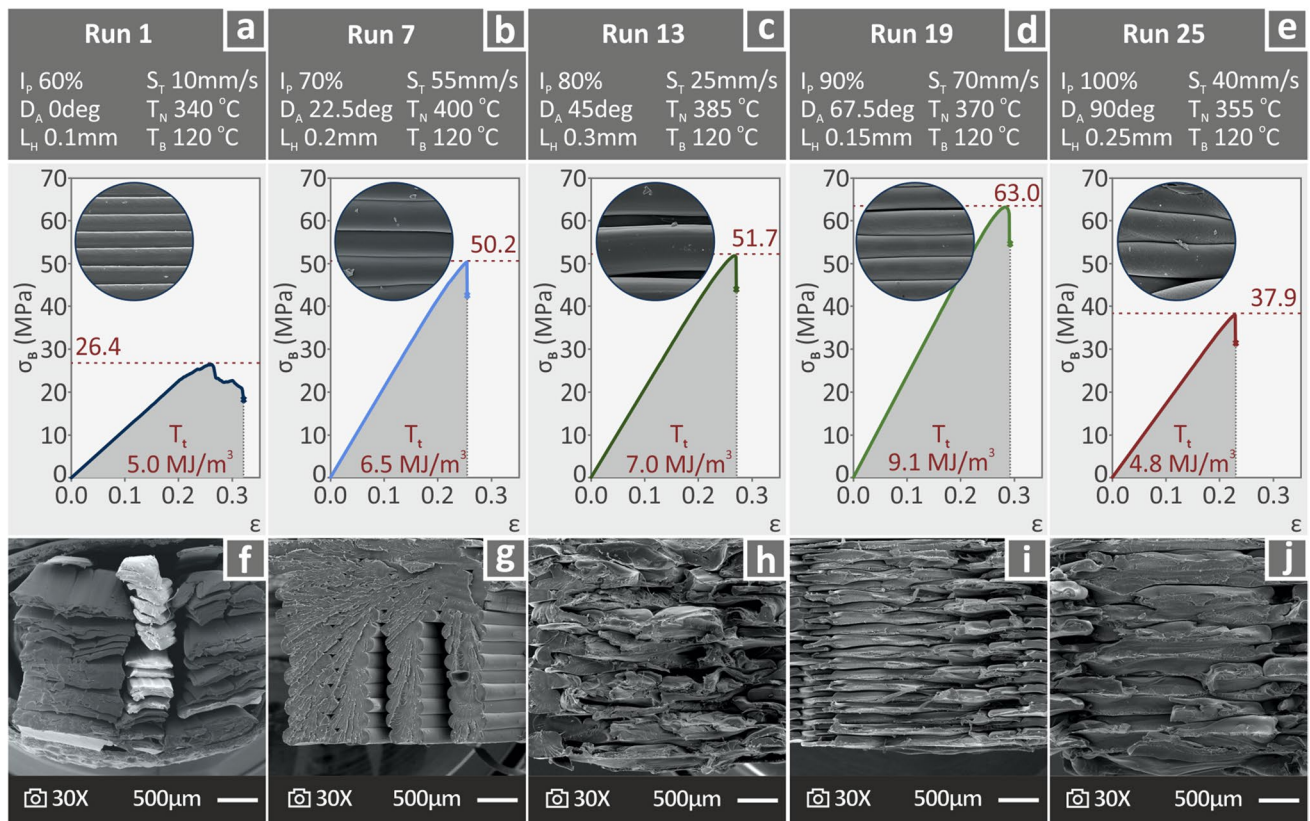
calculated as the integral of stress to strain. It is the area below the stress vs. strain curve. So, since run 19 exhibits the highest tensile strength and rather high strain at failure, it is normal to have the highest toughness. Run 1 shows the most ductile behavior with the highest strain at failure, but the strength is about half of that of run 19, so it is normal to have lower toughness than run 19.

Figure 5 shows microscopic images of the side surface of the 3D fabricated specimen (one selected out of the five samples made for each of the 25 runs), depicting their layer fusion. The printing time, tensile strength, and energy consumed (for fabrication with the 3D printing process) are also depicted in the images for each sample. Most of the samples present excellent fusion layering without gaps, voids, or bubbles, although there are still some cases such as runs 3, 4, 5, and 9, where some gaps appear, or runs 13, 22, and 25, where the layering is not well distributed.

Figure 6 shows stereoscopic images of the entire fracture surface of the 3DP specimens (one randomly selected among the five samples made for every run) and the values of printing time, tensile strength, and consumed energy during their fabrication. There are samples such as runs 14, 18, and 19

that seem to maintain a uniform surface and a large distribution of layering. However, in some of the runs (such as runs 6, 7, and 16), samples are presented with missing material parts and many hollows, possibly caused by the printing settings, which can affect the performance of the samples and require further investigation. Such defects may have enlarged during the failure of the parts in the tensile tests.

The fracture surface between a range of the selected specimens specifically runs 1, 7, 13, 19, and 25 (as explained above) was also investigated using SEM images at a higher magnification of 20 k $\times$ , as well as 80 k $\times$ . Images are presented along with the respective 3D printing parameters for each sample in Fig. 7a–e. The 80 k $\times$  magnification highlights the existence of bulges found at the fracture surface, which in some cases are also accompanied by pores, for example, run 7 (Fig. 7b). Overall, these high-magnification images highlight significant differences in the morphology of the samples at the microscale, arising from the variation in the 3D printing samples.



**Fig. 4** Graphs of stress versus strain, resulting from the tensile test, SEM images at  $\times 30$  magnification of **a** run 1, **b** run 7, **c** run 13, **d** run 19, and **e** run 25 sample side surfaces along with the conditions

under which they were built and the corresponding **f–j** fracture surface SEM images. The samples were selected according to the diagonal (Fig. 3), implying a total of 25 runs

### 3.2 Experimental results

Table 3 contains all the runs'  $\sigma_B$ ,  $E$ ,  $T_i$ , and  $W_S$  measured responses (average and standard deviation values) from each run's five replicates. All experimental measurements of  $\sigma_B$ ,  $E$ ,  $T_i$ , and  $W_S$  are shown in Table S5 in the supplementary information of this study, along with the corresponding values of the confirmation runs, which are shown in Table S7.

Table 4 contains the  $E_{PC}$ ,  $S_{PE}$ ,  $S_{PP}$ , and  $P_T$  measured responses (average and standard deviation values) from each run's five replicates. All experimental measurements of  $E_{PC}$ ,  $S_{PE}$ ,  $S_{PP}$ , and  $P_T$  are shown in Table S6 in the

supplementary information of this study, along with the corresponding values of the confirmation runs, which are shown in Table S8. Table 5 lists the control parameters for the infill percentage, deposition angle, layer height, travel speed, nozzle temperature, and bed temperature ranking for  $\sigma_B$ ,  $E$ ,  $T_i$ ,  $W_S$ ,  $E_{PC}$ ,  $S_{PE}$ ,  $S_{PP}$ , and  $P_T$ .

### 3.3 Statistical analysis

Figure 8 shows the box plots for the 3D printing time ( $P_T$ ) (s) versus travel speed ( $S_T$ ) and layer height ( $L_H$ ) (Fig. 8a), specimen weight ( $W_S$ ) (g) versus infill percentage ( $I_p$ ) and layer height ( $L_H$ ) (Fig. 8b), tensile strength ( $\sigma_B$ ) (MPa) versus



Fig. 5 Microscope images of the side surface of specimens for 25 runs. The 3D printing time, tensile strength, and energy for each sample are also presented



**Fig. 6** Stereoscope images from the specimen's fracture surface of the 25 runs (one randomly selected out of the five of each run). The printing time, tensile strength, and energy are also presented in every case

infill percentage ( $I_p$ ) and deposition angle ( $D_A$ ) (Fig. 8c), and overall energy consumption ( $E_{pC}$ ) (MJ) versus travel speed ( $S_T$ ) and layer height ( $L_H$ ) (Fig. 8d), created using the derived experimental results. The aim was to determine the most effective printing parameter for each response parameter. In the case of printing time and overall energy printing consumption, the values range between three or four values, while for specimen weight and tensile strength, the values are mostly scattered. This shows that there is a strong influence of the parameters, which leads to the need for deeper investigation and results analysis, as shown in Figs. 9, 10, 11, and 12.

All the response parameters were further analyzed and are presented in the main effect plots in Figs. 9, 10, 11, and 12. Out of the eight response-metrics evaluated, others need to satisfy “the lower the better criterion,” such as the printing time, weight, and energy metrics, while others need to satisfy “the higher the better criterion,” such as the tensile strength, Young’s modulus, and tensile toughness. The printing time and specimen weight are shown in Fig. 9. The increase in infill percentage does not affect  $P_T$  but causes a rise in  $W_S$  (rank no. 1,  $W_S$  values are excessively increased). The increase in the deposition angle, nozzle temperature, and bed temperature did not affect the



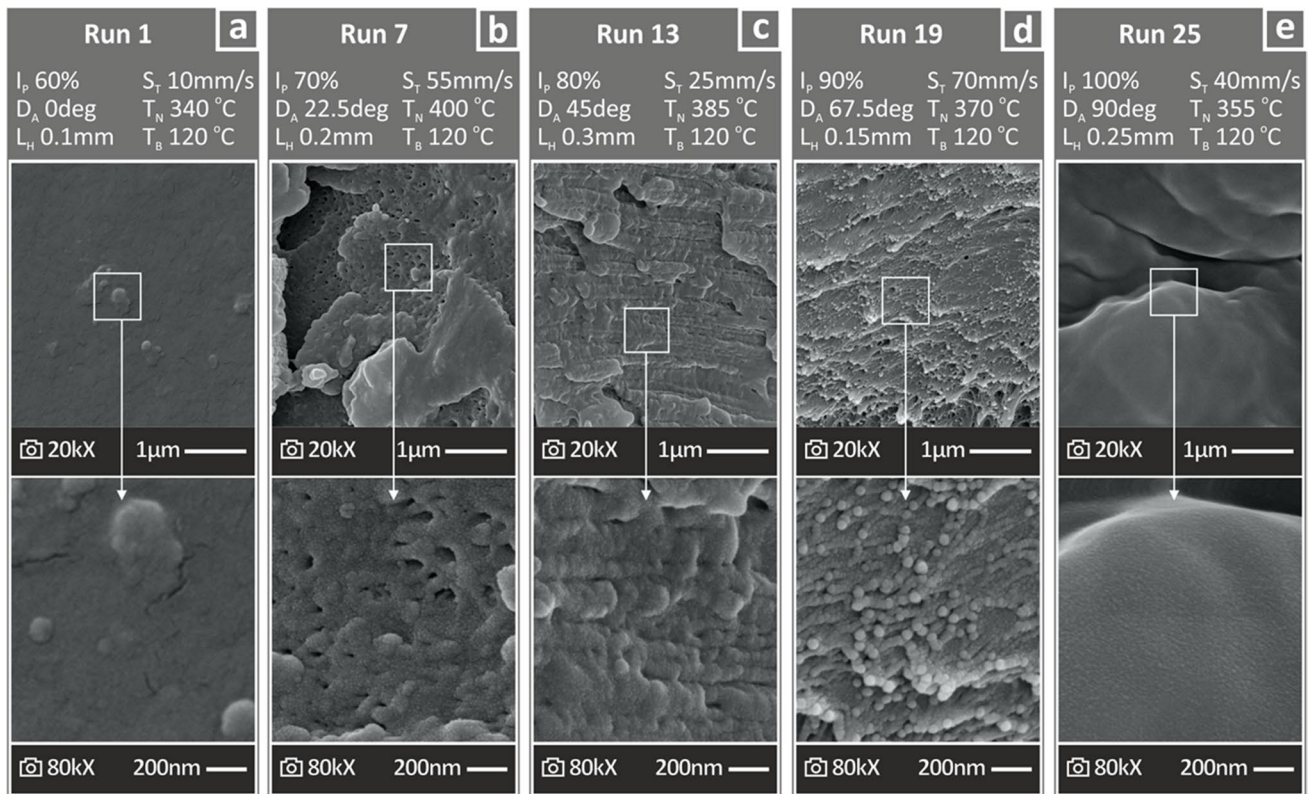


**Fig. 7** SEM images at 20 k× and 80 k× from the fracture surface of **a** run 1, **b** run 7, **c** run 13, **d** run 19, and **e** run 25 samples, along with the conditions under which they were built

$P_T$  and only caused a small increase in the  $W_S$ . The rise in layer height and travel speed seemed to cause a decrease in  $P_T$  (rank 2 and no. 1, respectively) and a rise in  $W_S$  (rank 2 and no. 5, respectively).

The tensile strength and overall energy consumption MEP are shown in Fig. 10. The increase in the infill percentage, nozzle temperature, and bed temperature increased  $\sigma_B$ , whereas the  $E_{PC}$  seemed to remain stable. An increase in the deposition angle decreased  $\sigma_B$  whereas the  $E_{PC}$  remained stable. As the layer’s height and travel speed increase,  $\sigma_B$  remains almost stable, and  $E_{PC}$  decreases. The infill density is ranked as the no. 1 parameter for  $\sigma_B$ , whereas the travel speed is ranked as the no. 1 parameter for  $E_{PC}$ . Only the travel speed caused significant changes in the  $E_{PC}$  values, whereas  $\sigma_B$  values remained rather stable only with the change in the layer height levels.

The MEP, presented in Fig. 11, shows the analysis of the tensile modulus of elasticity and tensile toughness response parameters. The increases in the infill percentage, nozzle temperature, and bed temperature increased both  $E$  and  $T_t$ . An increase in the deposition angle decreased both  $E$  and  $T_t$ . The height of the layer and the increase in travel

speed do not have an important influence on either  $E$  or  $T_t$  as they remain almost stable.

The specific printing energy and MEP are shown in Fig. 12. An increase in the infill percentage keeps the  $S_{PE}$  steady and decreases the  $S_{PP}$  (rank 2), while both the deposition angle and nozzle temperature maintain a steady response of the  $S_{PE}$  and  $S_{PP}$ . The layer height and travel speed cause a decrease in  $S_{PE}$  (rank no. 1) and maintain an  $S_{PP}$  within a small range of values, while during the increase in bed temperature,  $S_{PE}$  is steady and  $S_{PP}$  drastically rises (rank 1).

### 3.4 Regression analysis and analysis of variances (ANOVA)

The linear regression model (LRM) for each response is computed:

$$Y_k = a_k + \sum_{i=1}^n b_{i,k}x_i + e_k \tag{14}$$

while the reduced quadratic regression model (RQRM) for each response is computed:

**Table 3** Average as well as standard deviation values of the  $\sigma_B$ ,  $E$ ,  $T_t$ , and  $W_S$  responses

Run	$\sigma_B$ (MPa)	$E$ (MPa)	$T_t$ (MJ/m <sup>3</sup> )	$W_S$ (g)
1	24.23±4.49	108.79±4.57	4.51±1.33	1.06±0.06
2	15.74±0.48	88.12±4.61	2.63±0.35	1.22±0.01
3	20.03±0.63	101.09±10.92	3.57±0.54	1.38±0.03
4	23.96±0.49	120.20±4.46	3.67±0.19	1.38±0.00
5	31.05±0.53	156.12±3.48	3.59±0.12	1.43±0.03
6	63.19±0.68	243.84±9.70	10.45±1.99	1.36±0.02
7	43.27±5.55	202.45±8.03	5.06±1.03	1.49±0.03
8	30.18±3.39	148.33±9.19	3.77±0.53	1.45±0.02
9	29.91±4.82	143.05±9.58	4.12±0.04	1.58±0.01
10	25.05±0.97	153.00±2.39	2.40±0.48	1.43±0.01
11	77.20±0.96	238.84±7.48	17.56±2.59	1.48±0.03
12	69.42±7.54	240.56±21.59	11.48±1.53	1.57±0.02
13	50.93±3.19	194.42±10.27	7.44±0.80	1.79±0.01
14	37.07±4.30	222.22±6.15	3.30±0.54	1.61±0.01
15	34.25±5.01	169.89±12.69	3.81±0.33	1.52±0.00
16	80.73±2.96	250.95±7.65	17.84±0.89	1.77±0.07
17	64.10±2.39	222.05±2.45	10.79±0.80	1.70±0.06
18	74.68±1.65	282.07±21.71	10.68±1.03	1.58±0.02
19	54.22±6.46	222.68±11.18	7.26±1.45	1.68±0.06
20	61.10±3.52	248.20±4.87	7.62±1.20	1.68±0.03
21	65.19±7.25	235.28±14.97	11.32±0.87	1.72±0.16
22	71.20±2.06	265.14±14.60	11.79±0.54	1.80±0.01
23	68.28±6.63	272.29±4.20	9.76±2.27	1.69±0.02
24	52.21±6.74	215.25±9.77	7.74±1.36	1.82±0.06
25	35.33±2.84	172.95±1.00	4.23±0.53	1.79±0.05

**Table 4** Average and standard deviation values of measured responses for  $E_{PC}$ ,  $S_{PE}$ ,  $S_{PP}$ ,  $P_T$

Run	$E_{PC}$ (MJ)	$S_{PE}$ (MJ/g)	$S_{PP}$ (W/g)	$P_T$ (s)
1	0.871±0.016	0.821±0.043	288.8±15.1	2841.6±0.5
2	0.374±0.020	0.307±0.013	351.8±14.6	872.0±0.0
3	0.209±0.030	0.152±0.022	335.7±50.1	452.2±6.9
4	0.130±0.020	0.094±0.014	331.1±50.3	283.6±0.5
5	0.122±0.020	0.086±0.013	399.6±60.6	214.0±0.0
6	0.274±0.020	0.200±0.011	337.2±19.2	594.4±0.9
7	0.108±0.000	0.073±0.001	188.2±3.7	385.8±1.3
8	0.094±0.032	0.065±0.023	249.7±87.9	259.0±0.0
9	0.598±0.041	0.379±0.027	312.8±22.6	1212.4±0.5
10	0.662±0.020	0.462±0.014	328.8±9.5	1405.0±1.6
11	0.144±0.051	0.097±0.034	322.5±113.4	302.0±0.0
12	0.799±0.016	0.509±0.017	325.3±10.6	1565.6±0.5
13	0.194±0.032	0.109±0.018	191.6±32.8	568.8±5.2
14	0.454±0.020	0.282±0.011	264.7±10.2	1064.4±1.1
15	0.252±0.025	0.166±0.017	291.9±29.5	568.0±0.0
16	0.310±0.032	0.176±0.021	252.1±29.6	696.6±0.5
17	0.216±0.051	0.127±0.027	317.1±69.2	399.2±1.6
18	0.432±0.025	0.273±0.014	303.2±16.0	899.4±0.5
19	0.166±0.032	0.099±0.018	189.5±34.9	520.8±0.8
20	0.950±0.032	0.565±0.019	282.8±9.6	1998.4±0.5
21	0.115±0.016	0.067±0.008	227.6±27.8	295.6±0.5
22	0.353±0.030	0.196±0.016	267.3±22.2	731.6±0.5
23	1.440±0.000	0.852±0.012	305.1±4.2	2792.8±0.8
24	0.410±0.020	0.226±0.016	242.9±17.1	928.6±0.5
25	0.144±0.000	0.080±0.002	156.6±4.6	513.6±0.5

$$Y_k = a_k + \sum_{i=1}^n b_{i,k}x_i + \sum_{i=1}^n c_{i,k}x_i^2 + e_k \tag{15}$$

Finally, the full quadratic regression model (QRM), including the cross products of the settings, for each response was computed:

$$Y_k = a_{i,k} + \sum_{i=1}^n b_{i,k}x_i + \sum_{i=1}^n c_{i,k}x_i^2 + \sum_i \sum_j d_{ij,k}x_i x_j + e_k \tag{16}$$

where  $k$  stands for the response output (i.e.,  $\sigma_B$ ,  $E$ ,  $T_t$ ,  $E_{PC}$ ,  $S_{PE}$ ,  $S_{PP}$ ,  $W_S$ ,  $P_T$ ),  $a$  is a constant value,  $b$  corresponds to the coefficients of the linear terms,  $c$  represents the coefficients of the square terms,  $d$  is the coefficients of the two-way interaction terms,  $e$  is the error, and  $x_i$  represents the six ( $n=6$ ) control parameters (i.e.,  $I_p$ ,  $D_A$ ,  $L_H$ ,  $S_T$ ,  $T_N$ ,  $T_B$ ).

Regarding the polynomial ANOVA results:

- The  $\sigma_B$  factor has a 117.93  $F$  value and a 0.000  $P$  value, while the calculated values of the regression parameters

reach 90.88%. These results (Table 5) show the adequacy of Eq. 17 for forecasting the  $\sigma_B$  response factor.

- The  $E$  factor had an 84.21  $F$  value and a 0.000  $P$  value, while the calculated values of the regression parameters reached 78.98%. These results (Table 6) demonstrate the adequacy of Eq. 18 prediction model for forecasting the  $E$  response factor.
- The  $W_S$  factor has a 124.60  $F$  value and a  $P$  value of 0.000, while the calculated values of the regression parameters reach a percentage of 84.45%. These results (Table 7) demonstrate the adequacy of Eq. 19 prediction model for forecasting the  $W_S$  response factor.
- The  $P_T$  factor has a 128.57  $F$  value and a 0.000  $P$  value, while the calculated values of the regression parameters reach 91.56%. These results (Table 8) demonstrate the adequacy of Eq. 20 prediction model for forecasting the  $P_T$  response factor.

Additional polynomial ANOVA results regarding the  $T_t$ ,  $E_{PC}$ ,  $S_{PE}$ , and  $S_{PP}$  response factors, along with the

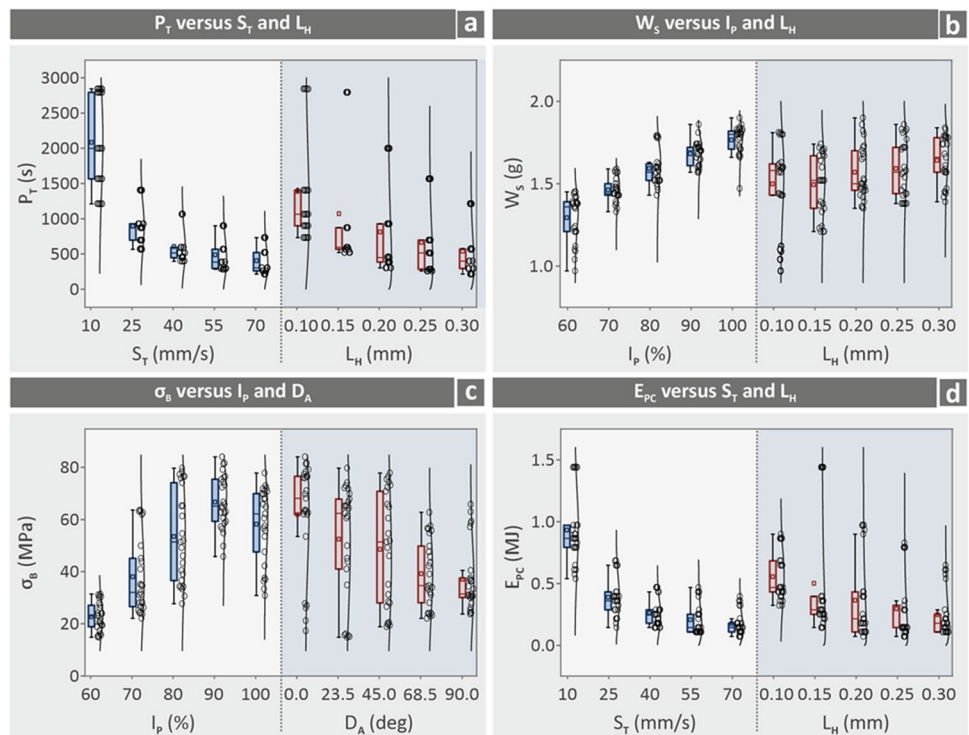
**Table 5** Control parameter ranking for  $\sigma_B$ ,  $E$ ,  $T_i$ ,  $W_S$ ,  $E_{PC}$ ,  $S_{PE}$ ,  $S_{PP}$ ,  $P_T$

Level	$I_p$ (%)	$D_A$ (deg)	$L_H$ (mm)	$S_T$ (mm/sec)	$T_N$ (°C)	$T_B$ (°C)
$\sigma_B$ (MPa)						
1	23	62.11	46.45	50.59	40.99	41.59
2	38.32	52.75	47.14	44.93	46.57	41.86
3	53.77	48.82	50.76	43.95	46.78	47.22
4	66.97	39.47	47.92	48.27	54.08	51.72
5	58.44	37.36	48.24	52.77	52.08	58.11
Delta	43.96	24.75	4.32	8.83	13.08	16.52
Rank	<b>1</b>	<b>2</b>	<b>6</b>	<b>5</b>	<b>4</b>	<b>3</b>
$E$ (MPa)						
1	114.9	215.5	206.2	202.6	172.9	180.3
2	178.1	203.7	199.4	180.3	185	188.4
3	213.2	199.6	201.2	192.4	190.5	186
4	245.2	184.7	186.6	202	214.4	201.3
5	232.2	180	190.2	206.2	220.8	227.6
Delta	130.3	35.5	19.6	25.9	47.9	47.3
Rank	<b>1</b>	<b>4</b>	<b>6</b>	<b>5</b>	<b>2</b>	<b>3</b>
$T_i$ (MJ/m <sup>3</sup> )						
1	3.594	12.338	6.534	7.498	6.124	5.701
2	5.161	8.35	6.782	7.609	7.846	5.728
3	8.718	7.042	8.311	6.468	7.206	8.226
4	10.838	5.218	8.199	6.907	8.192	8.835
5	8.967	4.33	7.452	8.795	7.911	8.788
Delta	7.244	8.007	1.777	2.327	2.068	3.135
Rank	<b>2</b>	<b>1</b>	<b>6</b>	<b>4</b>	<b>5</b>	<b>3</b>
$E_{PC}$ (MJ)						
1	0.3413	0.3427	0.5544	0.9317	0.3686	0.2966
2	0.347	0.3701	0.5011	0.3902	0.3384	0.3974
3	0.3686	0.4738	0.3643	0.2592	0.3902	0.3442
4	0.4147	0.3514	0.2952	0.2074	0.3802	0.5184
5	0.4925	0.4262	0.2491	0.1757	0.4867	0.4075
Delta	0.1512	0.131	0.3053	0.756	0.1483	0.2218
Rank	<b>4</b>	<b>6</b>	<b>2</b>	<b>1</b>	<b>5</b>	<b>3</b>
$S_{PE}$ (MJ/g)						
1	0.2917	0.2723	0.4065	0.6253	0.2806	0.2362
2	0.2358	0.2421	0.3248	0.2557	0.2273	0.2571
3	0.2326	0.29	0.2225	0.1682	0.2578	0.2136
4	0.2477	0.2158	0.1848	0.1345	0.2328	0.3264
5	0.2842	0.2717	0.1535	0.1084	0.2935	0.2587
Delta	0.0591	0.0742	0.253	0.5169	0.0662	0.1128
Rank	<b>6</b>	<b>4</b>	<b>2</b>	<b>1</b>	<b>5</b>	<b>3</b>
$S_{PP}$ (W/g)						
1	341.4	285.6	290.5	303	278.1	202.9
2	283.3	289.9	295.1	273.4	289.4	275.3
3	279.2	277	274.4	282.3	281.4	292
4	268.9	268.2	262.9	268.4	282	320.9
5	239.9	291.9	289.7	285.7	281.9	321.6
Delta	101.5	23.7	32.2	34.6	11.3	118.7
Rank	<b>2</b>	<b>5</b>	<b>4</b>	<b>3</b>	<b>6</b>	<b>1</b>
$W_S$ (g)						
1	1.294	1.478	1.499	1.516	1.512	1.561
2	1.462	1.557	1.494	1.606	1.53	1.536

**Table 5** (continued)

Level	$I_p$ (%)	$D_A$ (deg)	$L_H$ (mm)	$S_T$ (mm/sec)	$T_N$ (°C)	$T_B$ (°C)
3	1.593	1.577	1.569	1.569	1.554	1.608
4	1.682	1.613	1.592	1.538	1.603	1.537
5	1.765	1.572	1.642	1.568	1.597	1.554
Delta	0.471	0.135	0.148	0.089	0.092	0.073
Rank	<b>1</b>	<b>3</b>	<b>2</b>	<b>5</b>	<b>4</b>	<b>6</b>
$P_T$ (s)						
1	932.7	946	1388.4	2082.2	999.3	966.1
2	771.3	790.8	1069.6	894.2	759.9	897.9
3	813.8	994.4	813.4	604.8	847.8	732.2
4	902.9	802	663.7	486.5	835.4	1036.5
5	1052.4	939.8	538	405.5	1030.7	840.4
Delta	281.1	203.6	850.4	1676.7	270.8	304.4
Rank	<b>4</b>	<b>6</b>	<b>2</b>	<b>1</b>	<b>5</b>	<b>3</b>

**Fig. 8** Box plots for the **a** printing time ( $P_T$ ) versus travel speed ( $S_T$ ) and layer height ( $L_H$ ), **b** specimen weight ( $W_S$ ) versus infill percentage ( $I_p$ ) and layer height ( $L_H$ ), **c** tensile strength ( $\sigma_B$ ) versus infill percentage ( $I_p$ ) and deposition angle ( $D_A$ ), **d** overall energy printing consumption ( $E_{PC}$ ) versus travel speed ( $S_T$ ) and layer height ( $L_H$ )



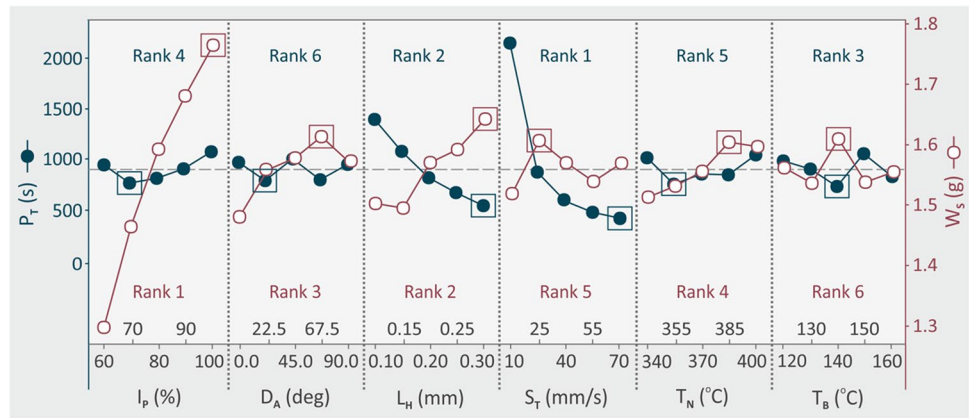
corresponding equations of the prediction model, can be found in the available supplementary information, Tables S3-S06 and Equation S1-S04, respectively.

Figure 13 shows the values of the predicted versus experimental data for the printing time (Fig. 13a), specimen weight (Fig. 13b), tensile strength (Fig. 13c), and overall energy consumption (Fig. 13d). The values in all cases appeared to range around the same acceptable deviation zone. Figure S2 in this work's supplementary information contains

interaction graphs that show how the control factors are linked with each other.

$$\begin{aligned}
 \sigma_B = & -565 + 6.703 \times I_p - 0.3942 \times D_A \\
 & + 91.2 \times L_H - 0.599 \times S_T + 2.09 \\
 & \times T_N - 1.846 \times T_B - 0.03567 \times I_p^2 \\
 & + 0.001280 \times D_A^2 - 206 \times L_H^2 \\
 & + 0.00813 \times S_T^2 - 0.00256 \times T_N^2 \\
 & + 0.00813 \times T_B^2
 \end{aligned} \quad (17)$$

**Fig. 9** Main effect plot of printing time ( $P_T$ ) and specimen weight ( $W_S$ ) versus the control settings of infill percentage ( $I_p$ ), deposition angle ( $D_A$ ), layer height ( $L_H$ ), travel speed ( $S_T$ ), nozzle temperature ( $T_N$ ) and bed temperature ( $T_B$ )



**Fig. 10** Main effect plot of tensile strength ( $\sigma_B$ ) and overall energy consumption ( $E_{PC}$ ) versus the control settings of infill percentage ( $I_p$ ), deposition angle ( $D_A$ ), layer height ( $L_H$ ), travel speed ( $S_T$ ), nozzle temperature ( $T_N$ ), and bed temperature ( $T_B$ )

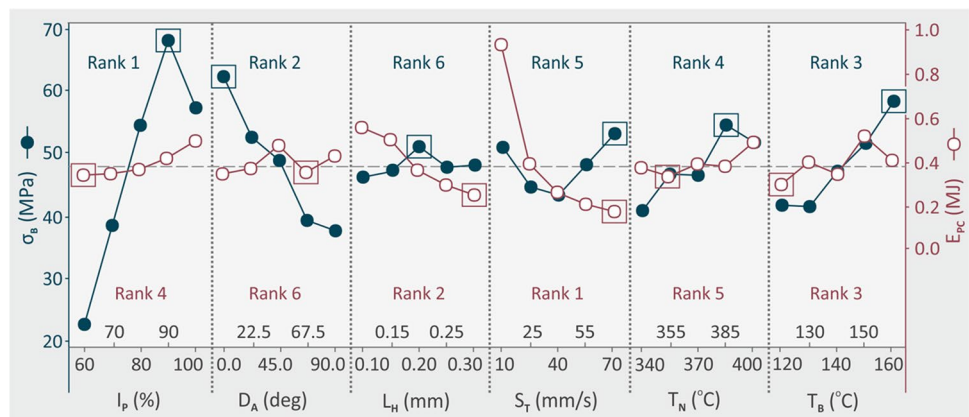
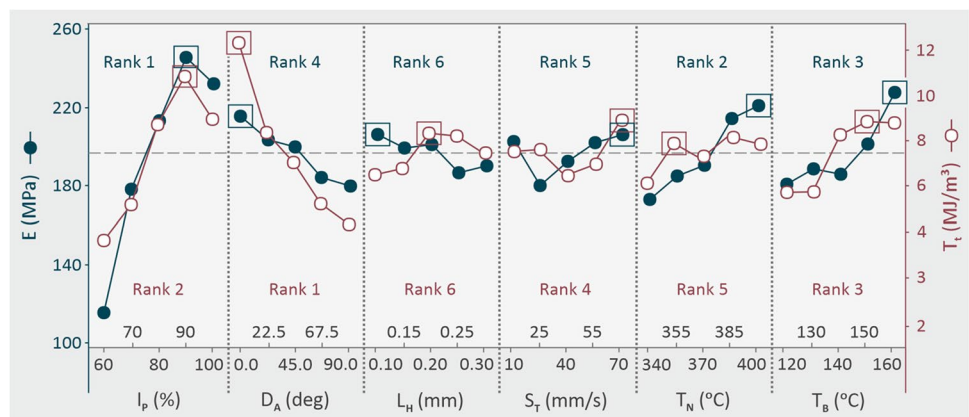


**Fig. 11** Main effect plot of tensile modulus of elasticity ( $E$ ) and tensile toughness ( $T_t$ ) versus the control settings of infill percentage ( $I_p$ ), deposition angle ( $D_A$ ), layer height ( $L_H$ ), travel speed ( $S_T$ ), nozzle temperature ( $T_N$ ), and bed temperature ( $T_B$ )



$$E = -475.8 + 3.017 \times I_p - 0.4000 \times D_A - 89.8 \times L_H + 0.193 \times S_T + 0.835 \times T_N + 1.075 \times T_B \quad (18)$$

$$W_S = -0.163 + 0.011612 \times I_p + 0.001084 \times D_A + 0.7664 \times L_H + 0.000229 \times S_T + 0.001624 \times T_N - 0.000132 \times T_B \quad (19)$$

**Fig. 12** Main effect plot of specific printing energy ( $S_{PE}$ ) and specific printing power ( $S_{PP}$ ) versus the control settings of infill percentage ( $I_P$ ), deposition angle ( $D_A$ ), layer height ( $L_H$ ), travel speed ( $S_T$ ), nozzle temperature ( $T_N$ ), and bed temperature ( $T_B$ )

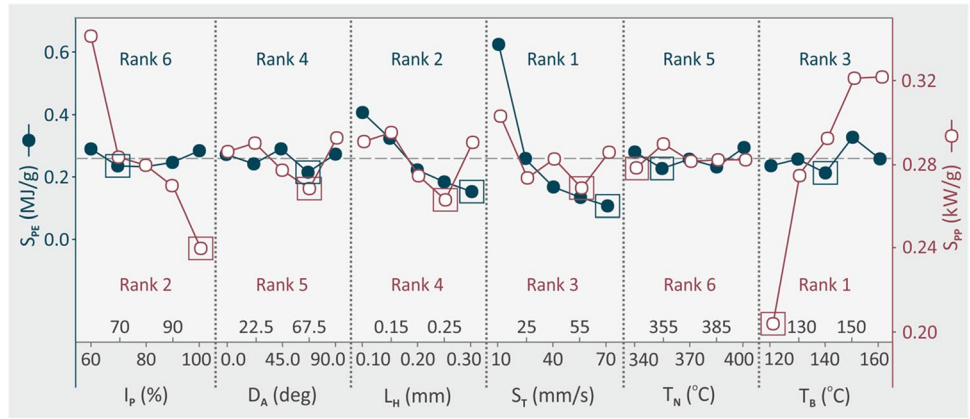


**Table 6** Polynomial ANOVA, RQRM,  $\sigma_B$  versus  $I_P$ ,  $D_A$ ,  $L_H$ ,  $S_T$ ,  $T_N$ ,  $T_B$

Source	$D_T$	Adj SS	Adj MS	F value	P value
Regression	12	47,825.6	3985.47	117.93	0.000
$I_P$	1	6109.6	6109.62	180.79	0.000
$D_A$	1	1582.3	1582.26	46.82	0.000
$L_H$	1	111.4	111.40	3.30	0.072
$S_T$	1	947.8	947.79	28.05	0.000
$T_N$	1	141.5	141.49	4.19	0.043
$T_B$	1	151.9	151.91	4.49	0.036
$I_P^2$	1	4454.3	4454.32	131.81	0.000
$D_A^2$	1	146.9	146.91	4.35	0.039
$L_H^2$	1	93.1	93.08	2.75	0.100
$S_T^2$	1	1172.3	1172.32	34.69	0.000
$T_N^2$	1	116.1	116.06	3.43	0.066
$T_B^2$	1	231.1	231.10	6.84	0.010
Error	112	3785.0	33.79		
Total	124				
$R^2$		92.67%			
$R^2$ (adj)		91.88%			
$R^2$ (pred)		90.88%			

$$\begin{aligned}
 P_T = & 42896 - 72.7 \times I_P - 2.42 \times D_A \\
 & - 9845 \times L_H - 85.65 \times S_T - 179.8 \\
 & \times T_N - 44.0 \times T_B + 0.478 \times I_P^2 \\
 & + 0.0268 \times D_A^2 + 14078 \times L_H^2 \\
 & + 0.7572 \times S_T^2 + 0.2442 \times T_N^2 \\
 & + 0.153 \times T_B^2
 \end{aligned}
 \tag{20}$$

Figure 14 presents 3D surface graphs of the response parameters versus the two control parameters that affect each other, showing their dependence. Figure 14a shows the printing time vs.  $S_T$  and  $L_H$ , Fig. 14b shows the tensile strength vs.  $I_P$  and  $D_A$ , Fig. 14c shows the overall energy printing consumption vs.  $S_T$  and  $L_H$ , Fig. 14d shows the specimen weight

**Table 7** Polynomial ANOVA, LRM,  $E$  vs  $I_P$ ,  $D_A$ ,  $L_H$ ,  $S_T$ ,  $T_N$ ,  $T_B$

Source	$D_T$	Adj SS	Adj MS	F value	P value
Regression	6	323,010	53,835	84.21	0.000
$I_P$	1	227,541	227,541	355.94	0.000
$D_A$	1	20,250	20,250	31.68	0.000
$L_H$	1	5036	5036	7.88	0.006
$S_T$	1	2090	2090	3.27	0.073
$T_N$	1	39,219	39,219	61.35	0.000
$T_B$	1	28,874	28,874	45.17	0.000
Error	118	75,433	639		
Total	124				
$R^2$		81.07%			
$R^2$ (adj)		80.11%			
$R^2$ (pred)		78.98%			

**Table 8** Polynomial ANOVA, LRM,  $W_S$  vs  $I_P$ ,  $D_A$ ,  $L_H$ ,  $S_T$ ,  $T_N$ ,  $T_B$

Source	$D_T$	Adj SS	Adj MS	F value	P value
Regression	6	4.03866	0.67311	124.60	0.000
$I_P$	1	3.37096	3.37096	623.99	0.000
$D_A$	1	0.14884	0.14884	27.55	0.000
$L_H$	1	0.36711	0.36711	67.95	0.000
$S_T$	1	0.00296	0.00296	0.55	0.461
$T_N$	1	0.14835	0.14835	27.46	0.000
$T_B$	1	0.00044	0.00044	0.08	0.777
Error	118	0.63746	0.00540		
Total	124				
$R^2$		86.37%			
$R^2$ (adj)		85.67%			
$R^2$ (pred)		84.45%			

vs.  $I_P$  and  $L_H$ , Fig. 14e shows the tensile strength vs.  $T_N$  and  $T_B$ , and Fig. 14f shows the overall energy printing consumption  $I_P$  and  $T_B$ .

**Fig. 13** Values of the predicted versus experimental data, **a** printing time ( $P_T$ ) (s), **b** specimen weight ( $W_s$ ) (mm/s), **c** tensile strength ( $\sigma_B$ ) (MPa), and **d** overall energy printing consumption ( $E_{PC}$ ) (MJ)

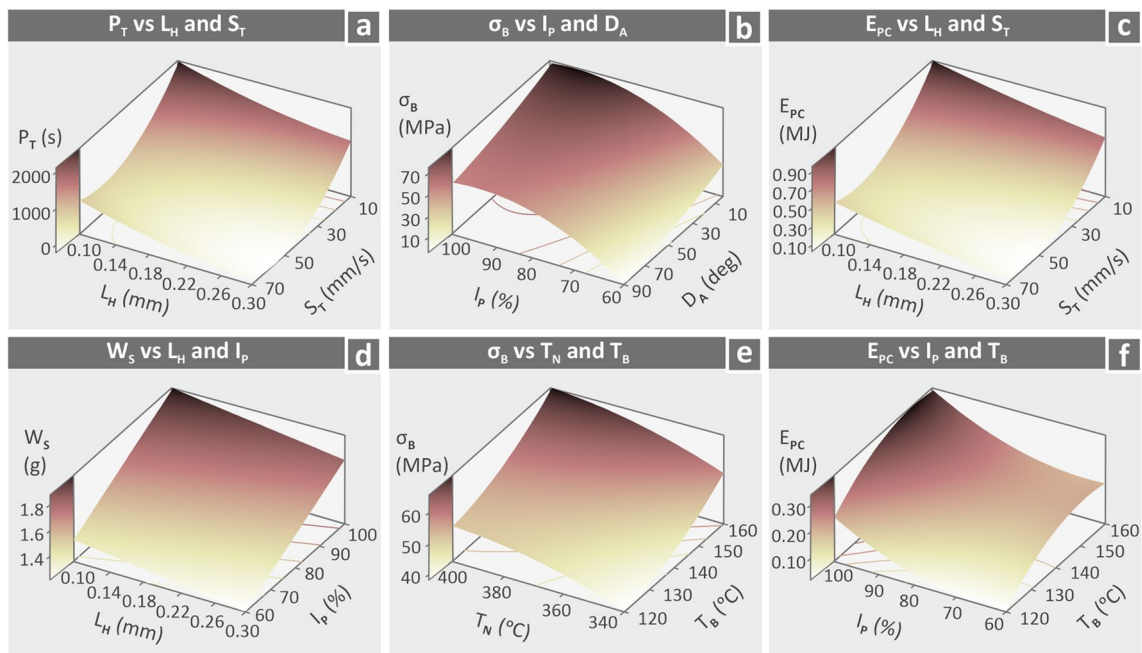
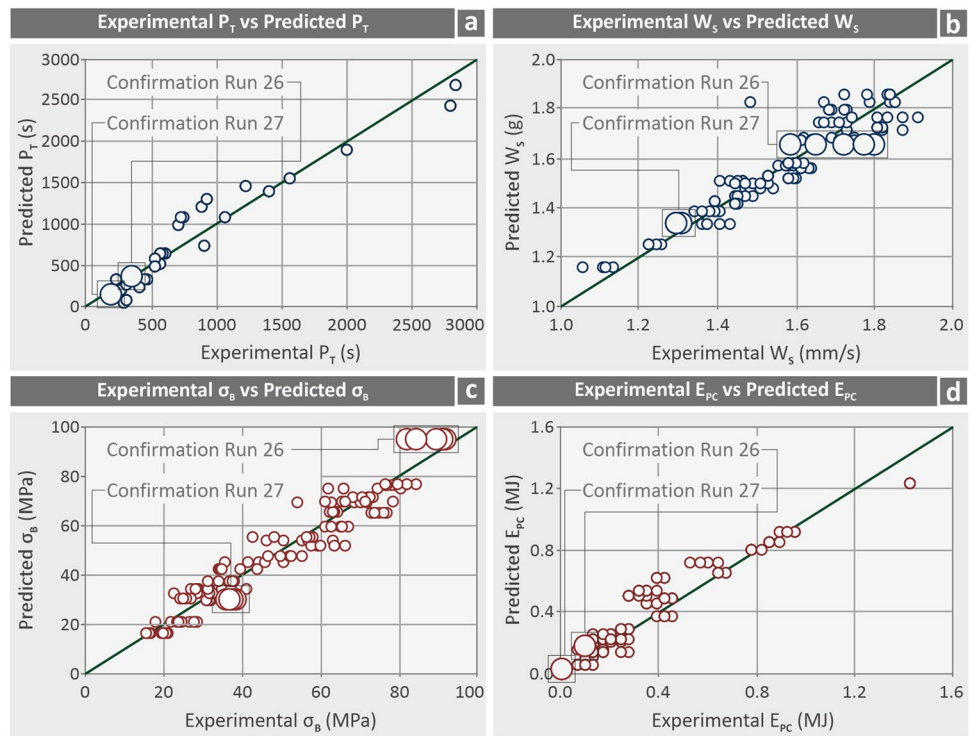


**Fig. 14** 3D surface plots of the **a** printing time ( $P_T$ ) versus travel speed ( $S_T$ ) and layer height ( $L_H$ ), **b** tensile strength ( $\sigma_B$ ) versus infill percentage ( $I_p$ ) and deposition angle ( $D_A$ ), **c** overall energy printing consumption ( $E_{PC}$ ) versus travel speed ( $S_T$ ) and layer height ( $L_H$ ), **d**

specimen weight ( $W_s$ ) versus infill percentage ( $I_p$ ) and layer height ( $L_H$ ), **e** tensile strength ( $\sigma_B$ ) versus nozzle temperature ( $T_N$ ) and bed temperature ( $T_B$ ), **f** overall energy printing consumption ( $E_{PC}$ ) versus infill percentage ( $I_p$ ) and bed temperature ( $T_B$ )

**Table 9** Polynomial ANOVA, RQRM,  $P_T$  vs  $I_P$ ,  $D_A$ ,  $L_H$ ,  $S_T$ ,  $T_N$ ,  $T_B$

Source	$D_T$	Adj SS	Adj MS	F value	P value
Regression	12	59,476,432	4,956,369	128.57	0.000
$I_P$	1	718,500	718,500	18.64	0.000
$D_A$	1	59,575	59,575	1.55	0.216
$L_H$	1	1,296,641	1,296,641	33.64	0.000
$S_T$	1	19,355,959	19,355,959	502.11	0.000
$T_N$	1	1,044,863	1,044,863	27.10	0.000
$T_B$	1	86,243	86,243	2.24	0.138
$I_P^2$	1	798,070	798,070	20.70	0.000
$D_A^2$	1	64,464	64,464	1.67	0.199
$L_H^2$	1	433,523	433,523	11.25	0.001
$S_T^2$	1	10,158,226	10,158,226	263.51	0.000
$T_N^2$	1	1,056,222	1,056,222	27.40	0.000
$T_B^2$	1	82,023	82,023	2.13	0.147
Error	112	4,317,546	38,550		
Total	124				
$R^2$	93.23%				
$R^2$ (adj)	92.51%				
$R^2$ (pred)	91.56%				

### 3.5 Confirmation experiments and validation

Two additional confirmation experimental runs were conducted with the aim of verifying the effectiveness of the prediction models, while there was also a correlation between the experimental findings and those calculated from the prediction models. The results of the control parameters are presented in Table 9, while the average and standard deviation values of the  $\sigma_B$ ,  $E$ ,  $T_t$ , and  $W_S$  measured responses of the confirmation runs are shown in Table 10, and the average and standard deviation values of the  $E_{PC}$ ,  $S_{PE}$ ,  $S_{PP}$ , and  $P_T$  measured responses for the confirmation runs are shown in Table 11. The analytical experimental results from each replica of the confirmation runs are presented in the Supplementary Information. Table 12 presents the deviations resulting from the experimental and predicted values that were obtained during this study. It should be highlighted that in the case of run 27, the values of the actual and predicted  $E_{PC}$  (MJ) coincide, as they do not present errors. The difference between the actual and predicted values of  $\sigma_B$  was small, and the error was low. For  $E_{PC}$ , the deviation was higher for run 26. Because the ANOVA showed that the reliability of the prediction model was high ( $R$  values higher than 89%, please see the supplementary information of the

**Table 10** Control parameters for the confirmation run

Run	$I_P$ (%)	$D_A$ (deg)	$L_H$ (mm)	$S_T$ (mm/sec)	$T_N$ (°C)	$T_B$ (°C)
26	90	0.0	0.20	70	385	160
27	60	0.0	0.30	70	355	120

**Table 11** Average and standard deviation values of measured responses for  $\sigma_B$ ,  $E$ ,  $T_t$ ,  $W_S$ , regarding confirmation runs

Run	$\sigma_B$ (MPa)	$E$ (MPa)	$T_t$ (MJ/m3)	$W_S$ (g)
26	87.51 ± 4.37	315.72 ± 22.93	11.14 ± 2.72	1.70 ± 0.09
27	36.89 ± 0.89	145.38 ± 3.76	12.20 ± 0.01	1.29 ± 0.01

**Table 12** Average and standard deviation values of measured responses for  $E_{PC}$ ,  $S_{PE}$ ,  $S_{PP}$ , and  $P_T$ , regarding confirmation runs

Run	$E_{PC}$ (MJ)	$S_{PE}$ (MJ/g)	$S_{PP}$ (W/g)	$P_T$ (s)
26	0.130 ± 0.000	0.042 ± 0.002	0.1 ± 0.0	332.6 ± 0.5
27	0.036 ± 0.000	0.028 ± 0.000	0.2 ± 0.0	177.6 ± 0.5

study), this deviation can be attributed to the specific set of control parameter levels. . Table 13

## 4 Discussion

This study presents the popular and generic settings (which were chosen as control parameters) for the mechanical response and energy consumption of PEI specimens fabricated using the MEX 3D printing method. The increased mechanical performance of 3D printed parts is a common demand in applications, while the energy consumption for the manufacturing of parts is related to their sustainability, which is also a popular subject nowadays. Six 3D printing settings were evaluated against eight response metrics to provide insight into their effects on the process for these two critical aspects (mechanical performance and energy consumption). The specimens were 3D printed and subjected to various experiments. The results were analyzed and validated using the Taguchi design method. The aim of this study was to compose a set of control parameters with optimal values while maintaining low energy consumption and a high yield of response parameters.

The mechanical behavior of the 3D fabricated parts was mostly influenced by the control parameter of the infill percentage, but it has not yet been investigated in the existing literature, to the best of the authors’ knowledge, and it has been proven to have a great impact on many of the response parameters. The infill percentage had the greatest impact on specimen weight. With the values range studied herein it varied from 1.3 to almost 1.8 g (~30%



**Table 13** Validation table

Run		26	27
Actual	$\sigma_B$ (MPa)	87.51	36.89
	$E_{PC}$ (MJ)	0.130	0.036
Predicted	$\sigma_B$ (MPa)	95.21	30.37
	$E_{PC}$ (MJ)	0.190	0.036
Absolute error	$\sigma_B$ (%)	8.8	17.7
	$E_{PC}$ (%)	46.6	Threshold reached

difference), without significantly influencing the required printing time.

Additionally, the  $I_p$  also influenced the tensile strength, which varied from approximately 22 to almost 70 MPa (~300%), again without a notable change in the energy demands. The tensile strength of 22 MPa corresponds to a common polymer strength in 3D printing (such as PLA [108]), rather than a high-performance polymer, such as PEI. The tensile strength is consistent with the expected mechanical properties of the high-performance PEI polymer in MEX 3D printing [73]. Such differences in the performance of the parts built with the MEX 3D printing method justify the need for such an analysis and optimization and provide valuable information when 3D printed parts are used for applications. Modulus of elasticity and tensile toughness were also increased by  $I_p$  at around 240 MPa (with the lowest reported value being around 115 MPa, more than 100% difference) and 12 MJ/m<sup>3</sup> (with the lowest reported value being around 3.8 MJ/m<sup>3</sup>, about 400% difference), respectively, while specific printing power dropped drastically below 0.24 kW/g without presenting high levels of specific printing energy consumption. The increase in travel speed lowered the printing time and caused a significant decrease in the energy printing consumption at 0.2 MJ, without influencing the weight of the specimens. The highest energy printing consumption reported with lower travel speed values was almost 0.95 MJ. This means that approximately one-fourth of the power was required to build parts with higher travel speeds than those with low ones. It was also observed that as the travel speed increased, the specific printing energy decreased.

The increase in both the nozzle and bed temperature only had a slight influence on the response parameters, except for the case where the bed temperature demanded a high amount of specific printing power (0.32 kW/g). This indicates that temperature does not have an important effect and sidesteps the study of Shelton et al. [69], which implies that the mechanical strength of the specimens depends highly on the envelope temperatures. It should be mentioned though that Ding et al. [73] proved that by increasing nozzle

temperature up to 390 °C, the tensile strength decreased and then increased again at temperatures above 400 °C, in this study the exact opposite is proved. It should be noted that the specimen weight did not show remarkable changes during the increase in control parameters, except for the infill percentage, which caused a drastic increase in specimen weight reaching almost 1.8 g, as already mentioned.

The deposition angle had a significant impact on the tensile strength without significant energy consumption. This increase lowered the tensile strength from over 60 to below 40 MPa, which complies with the research of Forés-Garriga et al. [71] They concluded with results showing that raster angle values higher than 0 °C presented lower tensile strength. A lowering of the modulus of elasticity to 180 MPa and tensile toughness to approximately 4 MJ/m<sup>3</sup> were also observed. Layer height increase was effective for lowering printing time at 500 s as well as specific printing energy at below 0.2 MJ/g, and slightly lowered the energy printing consumption, similar to the study of Pandelidi et al. [50] where the overall energy-printing consumption is also reduced. Table 14 presents a comparison of the current research tensile strength results with the literature. As shown, the presented results are in good agreement with the literature. Some studies present lower values and others higher values, within a reasonable range. Any differences can be attributed to the different grades used, different 3D printing settings and machines, and overall to the entire process followed. Additionally, some of the studies presented are investigating solid parts, not 3D printed ones, which, as expected, have higher strength than the 3D printed parts.

Overall, the results presented herein cannot be completely correlated with the literature, because no similar work so far, to the authors' knowledge, has investigated so many 3D printing parameters (six) simultaneously. To the best of the authors' knowledge, no study so far has examined the required energy for the manufacturing of parts made with high-performance PEI polymer in MEX 3D printing. As mentioned above, the findings of this study are consistent with the existing literature. As explained, specific parameters significantly affect the mechanical performance of the parts, whereas others affect the energy consumption. Therefore, these factors should be considered when 3D printing PEI parts using the MEX process.

The need for such an analysis and modeling of the experimental results was thus highly justified in the study, especially because similar research on high-performance polymers in MEX 3D printing is still limited. Unfortunately, no set of control parameter levels optimizes both the mechanical performance and energy consumption, but a balance between the two aspects can be found because parameters highly affecting one aspect in some cases have mild effects on the other. However, in applications with clear priorities toward one or the other aspect (mechanical performance or

**Table 14** Comparison of the tensile strength (MPa) results presented herein with the literature

Study herein	(El Magri et al., 2021) [5]	(Byberg et al., 2018) [42]	(Zhang & Ki Moon, 2021) [49]	(Pandelidi et al., 2021) [50]	(Zaldivar et al., 2017) [51]	(Chueca de Bruijn et al., 2022) [56]	(Yilmaz et al., 2022) [58]	(Gebisa and Lemu, 2019) [59]	(Glaskova-Kuzmina et al., 2023) [60]
80.73	100.0	89.0	88.0	94.2	71.03	61.0	75.11	87.0	68.1
(Padovano et al., 2020) [66]	(Han et al., 2019) [67]	(Kaplun et al., 2020) [68]	(Shelton et al., 2020) [69]	(Chueca de Bruijn et al., 2020) [72]	(Ding et al., 2019) [73]	(Ahmad & Ezdeen, 2023) [75]	(Fischer & Schöppner, 2017) [76]	(Bagsik et al., 2011) [77]	All values in (MPa)
73.0	82.0	101.5	87.1	64.82	135.0	140.0	50.6	84.0	

energy consumption), this study provides valuable information to achieve these goals. The compiled equations proved their reliability (by the calculated factors in the ANOVA and the confirmation runs) and provided both qualitative and quantitative information. These prediction models along with the optimization of the control parameters studied contribute to the sustainability and functionality of 3D-printed PEI products. As reported above, the energy consumed for the 3D printing of PEI parts can be reduced by ~400%, while the strength of the parts can be increased by ~300%. No set of control parameter values optimized both the energy consumption and the strength of the 3D printed PEI parts, still a balance between sustainability and performance can be found and values that lead to inferior sustainability and performance results can be avoided.

## 5 Conclusions

This study is related to the analysis and optimization of the mechanical performance and energy consumed (during the production) of parts made with the pure PEI high-performance polymer using the MEX 3D printing process. Subsequently, the energy demands were measured during the 3D printing process, and the produced samples were subjected to testing to determine their performance under uniaxial loading (tensile test) following the guidelines outlined in the ASTM D638-02a international standard. The Taguchi design was selected as the methodology for evaluating the interaction between the six printing/control factors and the intended yield of mechanical and energy qualities. The objective was to minimize energy consumption while maximizing mechanical performance. No set of parameters simultaneously maximizes the tensile strength and minimizes the energy consumption; therefore, the control parameter level should be selected according to the demands of each application. However, some parameters significantly affect the mechanical property metrics and

have a limited effect on the energy metrics, such as the deposition angle. Additionally, some parameters, such as the travel speed, increase the tensile strength and reduce the energy consumption. Such findings can achieve a balance between mechanical performance and energy consumption for specific applications. The increase in the infill density significantly increased the tensile strength of the samples, whereas the increase in travel speed significantly decreased the energy consumption. Therefore, it is feasible to find a set of control parameter levels to produce PEI parts with high mechanical performance using the MEX process, while simultaneously saving energy for their production at the same time.

Prediction models were formed with high confidence levels for all the metrics. Two confirmation runs were conducted to assess the reliability of the prediction models. The reliability of the prediction model for the tensile strength was fully confirmed, whereas the energy consumption model did not provide perfectly accurate results owing to the control parameter levels, showing the restrictions of the modeling process. In future work, the range of the control parameter levels can be broadened, and additional modeling approaches can be applied and compared for their effectiveness using specific experimental data. Additionally, additional mechanical tests can be performed. Nevertheless, the reliability of the prediction models makes them valuable tools for producing parts using the MEX 3D printing method with a high-performance PEI polymer.

**Supplementary Information** The online version contains supplementary material available at <https://doi.org/10.1007/s00170-024-13418-w>.

**Acknowledgements** The authors would like to thank the Institute of Electronic Structure and Laser of the Foundation for Research and Technology-Hellas (IESL-FORTH) and, in particular, Ms. Aleka Manousaki for obtaining the SEM images presented in this work.

**Funding** Open access funding provided by HEAL-Link Greece. This work was supported by the European Union's Horizon 2020 Research and Innovation Program under the EMERGE project. The EMERGE project received funding under Grant Agreement No. 101008701.

**Data availability** The raw/processed data required to reproduce these findings cannot be shared because of technical or time limitations.

## Declarations

**Competing interests** The authors declare no competing interests.

**Disclaimer** Funding sponsors had no role in the design of the study; collection, analysis, or interpretation of data; writing of the manuscript; or decision to publish the results. The journal policies have been reviewed and accepted by all authors.

**Open Access** This article is licensed under a Creative Commons Attribution 4.0 International License, which permits use, sharing, adaptation, distribution and reproduction in any medium or format, as long as you give appropriate credit to the original author(s) and the source, provide a link to the Creative Commons licence, and indicate if changes were made. The images or other third party material in this article are included in the article's Creative Commons licence, unless indicated otherwise in a credit line to the material. If material is not included in the article's Creative Commons licence and your intended use is not permitted by statutory regulation or exceeds the permitted use, you will need to obtain permission directly from the copyright holder. To view a copy of this licence, visit <http://creativecommons.org/licenses/by/4.0/>.

## References

- Pereira T, Kennedy JV, Potgieter J (2019) A comparison of traditional manufacturing vs additive manufacturing, the best method for the job. *Procedia Manuf* 30:11–18. <https://doi.org/10.1016/j.promfg.2019.02.003>
- Attaran M (2017) The rise of 3-D printing: the advantages of additive manufacturing over traditional manufacturing. *Bus Horiz* 60:677–688. <https://doi.org/10.1016/j.bushor.2017.05.011>
- Christopher A, De Leon C, Da Silva ÍGM et al (2021) High performance polymers for oil and gas applications. *React Funct Polym* 162:104878. <https://doi.org/10.1016/j.reactfunctpolym.2021.104878>
- Ferreira I, Machado M, Alves F, Torres Marques A (2019) A review on fibre reinforced composite printing via FFF. *Rapid Prototyp J* 25:972–988
- El Magri A, Vanaei S, Vaudreuil S (2021) An overview on the influence of process parameters through the characteristic of 3D-printed PEEK and PEI parts. *High Perform Polym* 33:862–880
- Johnson RO, Burlhis HS (1983) Polyetherimide: a new high-performance thermoplastic resin. *J Polym Sci Polym Symp* 70:129–143. <https://doi.org/10.1002/polc.5070700111>
- Panayotov IV, Orti V, Cuisinier F, Yachouh J (2016) Polyetheretherketone (PEEK) for medical applications. *J Mater Sci Mater Med* 27:118. <https://doi.org/10.1007/s10856-016-5731-4>
- Choupin T, Debertrand L, Fayolle B et al (2019) Influence of thermal history on the mechanical properties of poly(ether ketone ketone) copolymers. *Polym Crystalliz* 2:e10086. <https://doi.org/10.1002/pcr2.10086>
- L Quiroga Cortés N, Caussé E, Dantras et al (2016) Morphology and dynamical mechanical properties of poly ether ketone ketone (PEKK) with meta phenyl links *J Appl Polym Sci* 133. <https://doi.org/10.1002/app.43396>
- Saxena P, Shukla P (2021) A comprehensive review on fundamental properties and applications of poly(vinylidene fluoride) (PVDF). *Adv Compos Hybrid Mater* 4:8–26. <https://doi.org/10.1007/s42114-021-00217-0>
- Slonov A, Musov I, Zhansitov A et al (2022) Investigation of the properties of polyphenylene sulfone blends. *Materials* 15(18):6381. <https://doi.org/10.3390/ma15186381>
- Kiani S, Mousavi SM, Saljoughi E, Shahtahmassebi N (2018) Preparation and characterization of modified polyphenylsulfone membranes with hydrophilic property for filtration of aqueous media. *Polym Adv Technol* 29:1632–1648. <https://doi.org/10.1002/pat.4268>
- Sun H, Sur GS, Mark JE (2002) Microcellular foams from polyethersulfone and polyphenylsulfone: preparation and mechanical properties. *Eur Polym J* 38:2373–2381. [https://doi.org/10.1016/S0014-3057\(02\)00149-0](https://doi.org/10.1016/S0014-3057(02)00149-0)
- Zawaski C, Williams C (2020) Design of a low-cost, high-temperature inverted build environment to enable desktop-scale additive manufacturing of performance polymers. *Addit Manuf* 33. <https://doi.org/10.1016/j.addma.2020.101111>
- Teton ZE, Cheaney B, Obayashi JT, Than KD (2020) PEEK interbody devices for multilevel anterior cervical discectomy and fusion: association with more than 6-fold higher rates of pseudarthrosis compared to structural allograft. *J Neurosurg Spine SPI* 32:696–702. <https://doi.org/10.3171/2019.11.SPINE.19788>
- Johannes Karl Fink (2008) High performance polymers, second ed. William Andrew Publishing, Oxford
- Wiesli MG, Özcan M (2015) High-performance polymers and their potential application as medical and oral implant materials: a review. *Implant Dent* 24:448–457. <https://doi.org/10.1097/ID.0000000000000285>
- Panda JN, Bijwe J, Pandey RK (2017) Comparative potential assessment of solid lubricants on the performance of poly aryl ether ketone (PAEK) composites. *Wear* 384–385:192–202. <https://doi.org/10.1016/j.wear.2016.11.044>
- Weyhrich CW, Long TE (2022) Additive manufacturing of high-performance engineering polymers: present and future. *Polym Int* 71:532–536
- Chyr G, DeSimone JM (2022) Review of high-performance sustainable polymers in additive manufacturing. *Green Chem* 25:453–466
- De Leon AC, Chen Q, Palaganas NB et al (2016) High performance polymer nanocomposites for additive manufacturing applications. *React Funct Polym* 103:141–155
- Kishore V, Chen X, Ajinjeru C et al (2015) Additive manufacturing of high performance semicrystalline thermoplastics and their composites. 26th Annual International Solid Freeform Fabrication Symposium 906–915
- Vidakis N, Petousis M, Karapidakis E, et al (2023) Energy consumption versus strength in MEX 3D printing of polylactic acid. *Adv Indust Manuf Eng* 6. <https://doi.org/10.1016/j.aime.2023.100119>
- Petousis M, Vidakis N, Mountakis N et al (2023) Functionality versus sustainability for PLA in MEX 3D printing : the impact of generic process control factors on flexural response and energy efficiency. *Polymers (Basel)* 15:1232. <https://doi.org/10.3390/polym15051232>
- Petousis M, Vidakis N, Mountakis N et al (2023) Compressive response versus power consumption of acrylonitrile butadiene styrene in material extrusion additive manufacturing: the impact of seven critical control parameters. *Int J Adv Manuf Technol* 126:1233–1245. <https://doi.org/10.1007/s00170-023-11202-w>
- Vidakis N, Kechagias JD, Petousis M et al (2022) The effects of FFF 3D printing parameters on energy consumption. *Mater Manuf* 00:1–18. <https://doi.org/10.1080/10426914.2022.2105882>

27. Vidakis N, Petousis M, David CN et al (2023) Mechanical performance over energy expenditure in MEX 3D printing of polycarbonate : a multiparametric optimization with the aid of robust experimental design. *J Manuf Mater Process* 7:38. <https://doi.org/10.3390/jmmp7010038>
28. Vidakis N, Petousis M, Mountakis N et al (2023) Energy consumption vs. tensile strength of poly [methyl methacrylate ] in material extrusion 3D printing : the impact of six control settings. *Polymers (Basel)* 15:845. <https://doi.org/10.3390/polym15040845>
29. David C, Sagris D, Petousis M et al (2023) Operational performance and energy efficiency of MEX 3D printing with polyamide 6 (PA6): multi-objective optimization of seven control settings supported by L27 robust design. *Appl Sci* 13(15):8819. <https://doi.org/10.3390/app13158819>
30. Sekine C, Tsubata Y, Yamada T, et al (2014) Recent progress of high performance polymer OLED and OPV materials for organic printed electronics. *Sci Technol Adv Mater* 15. <https://doi.org/10.1088/1468-6996/15/3/034203>
31. Petousis M, Ntintakis I, David C et al (2023) A coherent assessment of the compressive strain rate response of PC, PETG, PMMA, and TPU thermoplastics in MEX additive manufacturing. *Polymers (Basel)* 15(19):3926. <https://doi.org/10.3390/polym15193926>
32. Kechagias JD, Vidakis N, Petousis M, Mountakis N (2022) A multi-parametric process evaluation of the mechanical response of PLA in FFF 3D printing. *Mater Manuf Processes* 00:1–13. <https://doi.org/10.1080/10426914.2022.2089895>
33. Kam M, İpekçi A, Şengül Ö (2021) Investigation of the effect of FDM process parameters on mechanical properties of 3D printed PA12 samples using Taguchi method. *J Thermoplast Compos Mater* 36:307–325. <https://doi.org/10.1177/08927057211006459>
34. Samykano M, Selvamani SK, Kadirgama K et al (2019) Mechanical property of FDM printed ABS: influence of printing parameters. *Intl J Adv Manuf Technol* 102:2779–2796. <https://doi.org/10.1007/s00170-019-03313-0>
35. Wang P, Zou B, Xiao H et al (2019) Effects of printing parameters of fused deposition modeling on mechanical properties, surface quality, and microstructure of PEEK. *J Mater Process Technol* 271:62–74. <https://doi.org/10.1016/j.jmatprotec.2019.03.016>
36. Ouassil S-E, El Magri A, Vanaei HR, Vaudreuil S (2023) Investigating the effect of printing conditions and annealing on the porosity and tensile behavior of 3D-printed polyetherimide material in Z-direction. *J Appl Polym Sci* 140:e53353. <https://doi.org/10.1002/app.53353>
37. Vidakis N, Petousis M, Mountakis N, Karapidakis E (2023) Box-Behnken modeling to quantify the impact of control parameters on the energy and tensile efficiency of PEEK in MEX 3D-printing. *Heliyon* 9:e18363. <https://doi.org/10.1016/j.heliyon.2023.e18363>
38. Garcia-Gonzalez D, Rodriguez-Millan M, Rusinek A, Arias A (2015) Investigation of mechanical impact behavior of short carbon-fiber-reinforced PEEK composites. *Compos Struct* 133:1116–1126. <https://doi.org/10.1016/j.compstruct.2015.08.028>
39. van de Werken N, Koirala P, Ghorbani J, et al (2021) Investigating the hot isostatic pressing of an additively manufactured continuous carbon fiber reinforced PEEK composite. *Addit Manuf* 37. <https://doi.org/10.1016/j.addma.2020.101634>
40. Ramgobin A, Fontaine G, Bourbigot S (2019) Thermal degradation and fire behavior of high performance polymers. *Polym Rev* 59:55–123
41. Bloomfield R, Crossman D, Raeissi A (1999) Using polyetherimide thermoplastic for forward lighting complex reflectors. *SAE Technical Paper* 3179. <https://doi.org/10.4271/1999-01-3179>
42. Byberg KI, Gebisa AW, Lemu HG (2018) Mechanical properties of ULTEM 9085 material processed by fused deposition modeling. *Polym Test* 72:335–347. <https://doi.org/10.1016/j.polymertesting.2018.10.040>
43. D'amore A, Caprino G, Nicolais L, Marino G (1999) Long-term behaviour of PEI and PEI-based composites subjected to physical aging. *Compos Sci Technol* 59:1993–2003. [https://doi.org/10.1016/S0266-3538\(99\)00058-5](https://doi.org/10.1016/S0266-3538(99)00058-5)
44. Bijwe J, Indumathi J, Ghosh AK (2002) Influence of weave of glass fabric on the oscillating wear performance of polyetherimide (PEI) composites. *Wear* 253:803–812. [https://doi.org/10.1016/S0043-1648\(02\)00167-9](https://doi.org/10.1016/S0043-1648(02)00167-9)
45. Zhao J, Wang C, Wang C, et al (2023) Significant enhancement of thermal conductivity and EMI shielding performance in PEI composites via constructing 3D microscopic continuous filler network. *Colloids Surf A Physicochem Eng Asp* 665. <https://doi.org/10.1016/j.colsurfa.2023.131222>
46. Yilmaz T, Sinmazcelik T (2010) Effects of hydrothermal aging on glass-fiber/polyetherimide (PEI) composites. *J Mater Sci* 45:399–404. <https://doi.org/10.1007/s10853-009-3954-1>
47. Rath T, Kumar S, Mahaling RN et al (2006) The flexible PEI composites. *Polym Compos* 27:533–538. <https://doi.org/10.1002/pc.20223>
48. Hajihi R, Baid H, Floyd S, et al (2020) Additive manufactured ULTEM 9085 part qualification and allowable generation. *SAMPE Virtual Conference Proceedings*. <https://doi.org/10.33599/nasampe/s.20.0364>
49. Zhang Y, Ki Moon S (2021) The effect of annealing on additive manufactured ultem™ 9085 mechanical properties. *Materials* 14. <https://doi.org/10.3390/ma14112907>
50. Pandelidi C, Maconachie T, Bateman S et al (2021) Parametric study on tensile and flexural properties of ULTEM 1010 specimens fabricated via FDM. *Rapid Prototyp J* 27:429–451. <https://doi.org/10.1108/RPJ-10-2019-0274>
51. Zaldivar RJ, Witkin DB, McLouth T et al (2017) Influence of processing and orientation print effects on the mechanical and thermal behavior of 3D-Printed ULTEM ® 9085 Material. *Addit Manuf* 13:71–80. <https://doi.org/10.1016/j.addma.2016.11.007>
52. Chueca de Bruijn A, Gómez-Gras G, Fernández-Ruano L et al (2023) Optimization of a combined thermal annealing and isostatic pressing process for mechanical and surface enhancement of Ultem FDM parts using Doehlert experimental designs. *J Manuf Process* 85:1096–1115. <https://doi.org/10.1016/j.jmapro.2022.12.027>
53. Parker ME, West M, Boysen A (2009) Eliminating voids in FDM processed polyphenylsulfone, polycarbonate, and ULTEM 9085 by hot isostatic pressing. *South Dakota School of Mines and Technology*
54. Taylor G, Wang X, Mason L et al (2018) Flexural behavior of additively manufactured Ultem 1010: experiment and simulation. *Rapid Prototyp J* 24:1003–1011. <https://doi.org/10.1108/RPJ-02-2018-0037>
55. Taylor G, Anandan S, Murphy D et al (2019) Fracture toughness of additively manufactured ULTEM 1010. *Virtual Phys Prototyp* 14:277–283. <https://doi.org/10.1080/17452759.2018.1558494>
56. Chueca de Bruijn A, Gómez-Gras G, Pérez MA (2022) Selective dissolution of polysulfone support material of fused filament fabricated Ultem 9085 parts. *Polym Test* 108. <https://doi.org/10.1016/j.polymertesting.2022.107495>
57. Yilmaz M, Yilmaz NF (2022) Effects of raster angle in single- and multi-oriented layers for the production of polyetherimide (PEI/ULTEM 1010) parts with fused deposition modelling. *Materialpruefung/Materials Testing* 64:1651–1661. <https://doi.org/10.1515/mt-2022-0085>
58. Yilmaz M, Yilmaz NF, Kalkan MF (2022) Rheology, crystallinity, and mechanical investigation of interlayer adhesion strength

- by thermal annealing of polyetherimide (PEI/ULTEM 1010) parts produced by 3D printing. *J Mater Eng Perform* 31:9900–9909. <https://doi.org/10.1007/s11665-022-07049-z>
59. Gebisa AW, Lemu HG (2019) Influence of 3D printing FDM process parameters on tensile property of ultem 9085. *Procedia Manuf* 30:331–338. <https://doi.org/10.1016/j.promfg.2019.02.047>
  60. Glaskova-Kuzmina T, Dejus D, Jātnieks J, et al (2023) Effect of post-printing cooling conditions on the properties of ULTEM printed parts. *Polymers (Basel)* 15. <https://doi.org/10.3390/polym15020324>
  61. Glaskova-Kuzmina T, Dejus D, Jātnieks J et al (2023) Effect of printing direction and post-printing conditions on bending properties of ULTEM 9085. *J Compos Sci* 7:316. <https://doi.org/10.3390/jcs7080316>
  62. Mzabi N, Smaoui H, Guerhazi H et al (2009) Heating effects on structural and electrical properties of polyetherimide. *Am J Eng Appl Sci* 2:120–126. <https://doi.org/10.3844/ajeas.2009.120.126>
  63. Fabrizio M, Strano M, Farioli D, Giberti H (2022) Extrusion additive manufacturing of PEI pellets. *J Manuf Mater Proc* 6. <https://doi.org/10.3390/jmmp6060157>
  64. Motaparti KP, Taylor G, Leu MC et al (2017) Experimental investigation of effects of build parameters on flexural properties in fused deposition modelling parts. *Virtual Phys Prototyp* 12:207–220. <https://doi.org/10.1080/17452759.2017.1314117>
  65. Gómez-Gras G, Pérez MA, Fábregas-Moreno J, Reyes-Pozo G (2021) Experimental study on the accuracy and surface quality of printed versus machined holes in PEI Ultem 9085 FDM specimens. *Rapid Prototyp J* 27:1–12. <https://doi.org/10.1108/RPJ-12-2019-0306>
  66. Padovano E, Galfione M, Concialdi P, et al (2020) Mechanical and thermal behavior of ultem® 9085 fabricated by fused-deposition modeling. *Appl Sci (Switzerland)* 10. <https://doi.org/10.3390/app10093170>
  67. Han P, Tofangchi A, Deshpande A et al (2019) An approach to improve interface healing in FFF-3D printed Ultem 1010 using laser pre-deposition heating. *Procedia Manuf* 34:672–677. <https://doi.org/10.1016/j.promfg.2019.06.195>
  68. Kaplun BW, Zhou R, Jones KW, et al (2020) Influence of orientation on mechanical properties for high-performance fused filament fabricated ultem 9085 and electro-statically dissipative polyetherketoneketone. *Addit Manuf* 36. <https://doi.org/10.1016/j.addma.2020.101527>
  69. Shelton TE, Willburn ZA, Hartsfield CR, et al (2020) Effects of thermal process parameters on mechanical interlayer strength for additively manufactured Ultem 9085. *Polym Test* 81. <https://doi.org/10.1016/j.polymertesting.2019.106255>
  70. Zaldivar RJ, Mclouth TD, Ferrelli GL et al (2018) Effect of initial filament moisture content on the microstructure and mechanical performance of ULTEM ® 9085 3D printed parts. *Addit Manuf* 24:457–466. <https://doi.org/10.1016/j.addma.2018.10.022>
  71. Forés-Garriga A, Pérez MA, Gómez-Gras G, Reyes-Pozo G (2020) Role of infill parameters on the mechanical performance and weight reduction of PEI Ultem processed by FFF. *Mater Des* 193. <https://doi.org/10.1016/j.matdes.2020.108810>
  72. Chueca de Bruijn A, Gómez-Gras G, Pérez MA (2020) Mechanical study on the impact of an effective solvent support-removal methodology for FDM Ultem 9085 parts. *Polym Test* 85. <https://doi.org/10.1016/j.polymertesting.2020.106433>
  73. Ding S, Zou B, Wang P, Ding H (2019) Effects of nozzle temperature and building orientation on mechanical properties and microstructure of PEEK and PEI printed by 3D-FDM. *Polym Test* 78. <https://doi.org/10.1016/j.polymertesting.2019.105948>
  74. McLouth TD, Gustafson SM, Kim HI, Zaldivar RJ (2021) Enhancement of FDM ULTEM® 9085 bond strength via atmospheric plasma treatment. *J Manuf Process* 66:179–188. <https://doi.org/10.1016/j.jmapro.2021.04.021>
  75. Ahmad SM, Ezdeen SY (2023) Effect of coating on the specific properties and damping loss factor of ULTEM 1010. *Zanco J Pure Appl Sci* 33:105–116
  76. Fischer M, Schöppner V (2017) Fatigue behavior of FDM parts manufactured with Ultem 9085. *JOM* 69:563–568. <https://doi.org/10.1007/s11837-016-2197-2>
  77. Bagsik A, Schöppner V (2011) Mechanical properties of fused deposition modeling parts manufactured with Ultem® 9085. In: *Proceedings of the 69th Annual Technical Conference of the Society of Plastics Engineers (ANTEC'11)*. Boston, MA, USA, pp 1194–1198
  78. Krause E, Yang GM, Sessler GM (1998) Charge dynamics and morphology of ultem 1000 and ultem 5000 PEI grade films. *Polym Int* 46:59–64
  79. Vidakis N, Petousis M, Kechagias JD (2022) A comprehensive investigation of the 3D printing parameters' effects on the mechanical response of polycarbonate in fused filament fabrication. *Progr Addit Manuf* 7:713–722. <https://doi.org/10.1007/s40964-021-00258-3>
  80. Vidakis N, Petousis M, Kechagias JD (2022) Parameter effects and process modelling of Polyamide 12 3D-printed parts strength and toughness. *Mater Manuf Processes* 37:1358–1369. <https://doi.org/10.1080/10426914.2022.2030871>
  81. Kechagias JD, Vidakis N, Petousis M (2021) Parameter effects and process modeling of FFF-TPU mechanical response. *Mater Manuf Processes*. <https://doi.org/10.1080/10426914.2021.2001523>
  82. Petousis M, Ninikas K, Vidakis N et al (2023) Multifunctional PLA/CNTs nanocomposites hybrid 3D printing integrating material extrusion and CO2 laser cutting. *J Manuf Process* 86:237–252. <https://doi.org/10.1016/j.jmapro.2022.12.060>
  83. Yang WH, Tarn YS (1998) Design optimization of cutting parameters for turning operations based on the Taguchi method. *J Mater Process Technol* 84:122–129. [https://doi.org/10.1016/S0924-0136\(98\)00079-X](https://doi.org/10.1016/S0924-0136(98)00079-X)
  84. Ning M, Mengjie S, Mingyin C et al (2016) Computational fluid dynamics (CFD) modelling of air flow field, mean age of air and CO2 distributions inside a bedroom with different heights of conditioned air supply outlet. *Appl Energy* 164:906–915. <https://doi.org/10.1016/j.apenergy.2015.10.096>
  85. Niu B, Shi M, Zhang Z et al (2022) Multi-objective optimization of supply air jet enhancing airflow uniformity in data center with Taguchi-based grey relational analysis. *Build Environ* 208:108606. <https://doi.org/10.1016/j.buildenv.2021.108606>
  86. Tutar M, Aydin H, Yuce C et al (2014) The optimisation of process parameters for friction stir spot-welded AA3003-H12 aluminium alloy using a Taguchi orthogonal array. *Mater Des* 63:789–797. <https://doi.org/10.1016/j.matdes.2014.07.003>
  87. Özel S, Vural E, Binici M (2020) Optimization of the effect of thermal barrier coating (TBC) on diesel engine performance by Taguchi method. *Fuel* 263:116537. <https://doi.org/10.1016/j.fuel.2019.116537>
  88. Pinar AM, Uluer O, Kirmaci V (2009) Optimization of counter flow Ranque-Hilsch vortex tube performance using Taguchi method. *Int J Refrig* 32:1487–1494. <https://doi.org/10.1016/j.ijrefrig.2009.02.018>
  89. Chang C-W, Kuo C-P (2007) Evaluation of surface roughness in laser-assisted machining of aluminum oxide ceramics with Taguchi method. *Int J Mach Tools Manuf* 47:141–147. <https://doi.org/10.1016/j.ijmactools.2006.02.009>
  90. Arslanoglu N, Yigit A (2016) Experimental investigation of radiation effect on human thermal comfort by Taguchi method. *Appl Therm Eng* 92:18–23. <https://doi.org/10.1016/j.applthermaleng.2015.09.070>
  91. Do KK, Choi DW, Choa Y-H, Kim HT (2007) Optimization of parameters for the synthesis of zinc oxide nanoparticles by

- Taguchi robust design method. *Colloids Surf A Physicochem Eng Asp* 311:170–173. <https://doi.org/10.1016/j.colsurfa.2007.06.017>
92. Arslanoglu N, Yigit A (2017) Investigation of efficient parameters on optimum insulation thickness based on theoretical-Taguchi combined method. *Environ Prog Sustain Energy* 36:1824–1831. <https://doi.org/10.1002/ep.12628>
93. Vidakis N, Petousis M, David CN et al (2023) Biomedical resin reinforced with cellulose nanofibers (CNF) in VAT photopolymerization (VPP) additive manufacturing (AM): the effect of filler loading and process control parameters on critical quality indicators (CQIs). *J Manuf Process* 101:755–769. <https://doi.org/10.1016/j.jmapro.2023.06.018>
94. Vidakis N, Petousis M, Mountakis N, et al (2023) Mechanical strength predictability of full factorial, Taguchi, and Box Behnken designs: optimization of thermal settings and Cellulose Nanofibers content in PA12 for MEX AM. *J Mech Behav Biomed Mater* 142. <https://doi.org/10.1016/j.jmbbm.2023.105846>
95. Vidakis N, Petousis M, Mountakis N, Kechagias JD (2022) Optimization of friction stir welding parameters in hybrid additive manufacturing: weldability of 3D-printed poly(methyl methacrylate) plates. *J Manuf Mater Proc* 6. <https://doi.org/10.3390/jmmp6040077>
96. Vidakis N, Petousis M, Mountakis N, et al (2022) Mechanical response assessment of antibacterial PA12/TiO<sub>2</sub> 3D printed parts: parameters optimization through artificial neural networks modeling. *Intl J Adv Manuf Technol* 785–803. <https://doi.org/10.1007/s00170-022-09376-w>
97. Kechagias JD, Tsiolikas A, Petousis M et al (2022) A robust methodology for optimizing the topology and the learning parameters of an ANN for accurate predictions of laser-cut edges surface roughness. *Simul Model Pract Theory* 114:102414. <https://doi.org/10.1016/j.simpat.2021.102414>
98. Kopar M, Yıldız AR (2023) Experimental investigation of mechanical properties of PLA, ABS, and PETG 3-d printing materials using fused deposition modeling technique. 65:1795–1804. <https://doi.org/10.1515/mt-2023-0202>
99. Günaydın AC, Yıldız AR, Kaya N (2022) Multi-objective optimization of build orientation considering support structure volume and build time in laser powder bed fusion. 64:323–338. <https://doi.org/10.1515/mt-2021-2075>
100. Aslan B, Yıldız AR (2020) Optimum design of automobile components using lattice structures for additive manufacturing. 62:633–639. <https://doi.org/10.3139/120.111527>
101. Simpson JR (1996) Taguchi techniques for quality engineering. *J Qual Technol* 28:487–489. <https://doi.org/10.1080/00224065.1996.11979713>
102. Bademlioglu AH, Canbolat AS, Yamankaradeniz N, Kaynakli O (2018) Investigation of parameters affecting Organic Rankine Cycle efficiency by using Taguchi and ANOVA methods. *Appl Therm Eng* 145:221–228. <https://doi.org/10.1016/j.applthermaleng.2018.09.032>
103. Palanikumar K (2011) Experimental investigation and optimisation in drilling of GFRP composites. *Measurement* 44:2138–2148. <https://doi.org/10.1016/j.measurement.2011.07.023>
104. Soni A, Patel RM, Kumar K, Pareek K (2022) Optimization for maximum extraction of solder from waste PCBs through grey relational analysis and Taguchi technique. *Miner Eng* 175:107294. <https://doi.org/10.1016/j.mineng.2021.107294>
105. Vidakis N, David C, Petousis M, et al (2022) The effect of six key process control parameters on the surface roughness, dimensional accuracy, and porosity in material extrusion 3D printing of polylactic acid: prediction models and optimization supported by robust design analysis. *Adv Indust Manuf Eng* 5. <https://doi.org/10.1016/j.aime.2022.100104>
106. Vidakis N, David C, Petousis M, et al (2023) Optimization of key quality indicators in material extrusion 3D printing of acrylonitrile butadiene styrene: the impact of critical process control parameters on the surface roughness, dimensional accuracy, and porosity. *Mater Today Commun* 34. <https://doi.org/10.1016/j.mtcomm.2022.105171>
107. Vidal C, Infante V, Peças P, Vilaça P (2013) Application of Taguchi method in the optimization of friction stir welding parameters of an aeronautic aluminium alloy. *Intl J Adv Mater Manuf Characteriz* 3:21–26. <https://doi.org/10.11127/ijammc.2013.02.005>
108. Hsueh M-H, Lai C-J, Wang S-H, et al (2021) Effect of printing parameters on the thermal and mechanical properties of 3D-printed PLA and PETG, using fused deposition modeling. *Polymers (Basel)* 13. <https://doi.org/10.3390/polym13111758>

**Publisher's Note** Springer Nature remains neutral with regard to jurisdictional claims in published maps and institutional affiliations.